

Evidence for bootstrap percolation dynamics in a photo-induced phase transition

Tyler Carbin,^{1,*} Xinshu Zhang,¹ Adrian B. Culver,^{1,2} Hengdi Zhao,³ Alfred Zong,^{4,5}
Rishi Acharya,¹ Cecilia J. Abbamonte,¹ Rahul Roy,^{1,2} Gang Cao,³ and Anshul Kogar^{1,†}

¹*Department of Physics and Astronomy, University of California Los Angeles, Los Angeles, CA 90095-1547*

²*Mani L. Bhaumik Institute for Theoretical Physics, Department of Physics and Astronomy,
University of California Los Angeles, Los Angeles, CA 90095*

³*Department of Physics, University of Colorado at Boulder, Boulder, Colorado 80309, USA*

⁴*Department of Chemistry, University of California at Berkeley, Berkeley, CA, 94720, USA*

⁵*Materials Sciences Division, Lawrence Berkeley National Laboratory, Berkeley, CA, 94720, USA*

(Dated: May 10, 2023)

Upon intense femtosecond photo-excitation, a many-body system can undergo a phase transition through a non-equilibrium route, but understanding these pathways remains an outstanding challenge. Here, we use time-resolved second harmonic generation to investigate a photo-induced phase transition in $\text{Ca}_3\text{Ru}_2\text{O}_7$ and show that mesoscale inhomogeneity profoundly influences the transition dynamics. We observe a marked slowing down of the characteristic time, τ , that quantifies the transition between two structures. τ evolves non-monotonically as a function of photo-excitation fluence, rising from below 200 fs to ~ 1.4 ps, then falling again to below 200 fs. To account for the observed behavior, we perform a bootstrap percolation simulation that demonstrates how local structural interactions govern the transition kinetics. Our work highlights the importance of percolating mesoscale inhomogeneity in the dynamics of photo-induced phase transitions and provides a model that may be useful for understanding such transitions more broadly.

In a photo-induced phase transition (PIPT), a qualitative and macroscopic change to the behavior of a many-body system occurs following intense femtosecond photo-excitation. PIPTs are inherently different from equilibrium transitions because they typically proceed through a far from equilibrium, non-thermal pathway where time becomes a fundamental variable. Tracking the temporal evolution of the spatially averaged response functions is crucial to understanding the spectacular behaviors instigated by photo-excitation in solids, such as the appearance of transient order and metastability of hidden states [1–6]. However, order often evolves in a spatially non-uniform manner in many PIPTs; a major recurring theme is the presence of electronic and crystallographic inhomogeneity on the nano- to micro-scale [7–25].

Experimentally capturing the *dynamics* of mesoscale structures has proven difficult. However, inhomogeneous textures have been observed in materials exhibiting long-lived metastability following photo-excitation. In the metastable “hidden” states of both $1T$ - TaS_2 [1, 26, 27] and strained $\text{La}_{2/3}\text{Ca}_{1/3}\text{MnO}_3$ [2, 28], quasi-static textures were observed using real-space scanning probe techniques. But, such experimental approaches are currently unfeasible for observing inhomogeneity that evolves on the short timescales characteristic of many PIPTs. A notable exception is the insulator-metal PIPT in VO_2 , which was found to exhibit similar transient textures determined by grain boundaries or pre-existing domains following each applied laser pulse [13, 14, 16]. To understand the effects of the dynamic inhomogeneity, our approach here is to quantify its aggregate effects on macroscopic observables and correlate the observations with a percolation model.

To accomplish this goal, we employ time-resolved second harmonic generation (SHG) to investigate a PIPT in a prototypical correlated material, $\text{Ca}_3\text{Ru}_2\text{O}_7$ (CRO), in which photo-induced inhomogeneity is expected to occur (see below). By relating the experimental observations to simulation results, we provide strong evidence that structural percolation, mediated by lattice strain, governs the transition kinetics. Specifically, we show that the photo-induced dynamics are consistent with bootstrap percolation (BP), a particular cellular automata model that lacks detailed balance.

$\text{Ca}_3\text{Ru}_2\text{O}_7$ (CRO) is the $n=2$ compound in the Ruddlesden-Popper series $\text{Ca}_{n+1}\text{Ru}_n\text{O}_{3n+1}$ [29]. The crystal is distorted from the typical $I4/mmm$ structure due to rotation and tilts of the oxygen octahedra around the (001) axis and (110) axis, respectively (Fig. 1(b)). At all temperatures, its crystallographic space group is $Bb2_1m$ (No. 36), with point group C_{2v} . As the temperature is reduced below the Néel temperature, $T_N=56$ K, CRO undergoes a continuous phase transition to an antiferromagnetic state in which the Ru spins are aligned ferromagnetically along the $\pm a$ axis within each bilayer and antiferromagnetically between bilayers [30]. Of primary interest here is the discontinuous metal-insulator transition at $T_{MI}=48$ K. In samples grown by the floating zone method, the low-temperature state is semimetallic [31–33], but in the flux-grown samples used here, this state is truly insulating [34]. This electronic transition is accompanied by a rotation of the spins from the $\pm a$ axis to the $\pm b$ axis [30, 35] and a structural transition without a change in crystallographic symmetry. Through the transition, the c axis contracts by $\sim 0.1\%$ and the a and b axis lattice parameters expand by $\sim 0.07\%$ [29]. The

structural change leads to a compression of the oxygen octahedra and further breaks the degeneracy between the Ru d_{xy} and the $d_{xz/yz}$ orbitals; it is therefore thought to be a vital component of the insulator-metal transition by promoting an orbital polarization [35–39].

To probe the dynamics of the phase transition, we perform time-resolved SHG, a technique that can monitor the symmetry of CRO in its various phases [40]. These measurements were performed in a reflection geometry, using 180 fs laser pulses with a 5 kHz repetition rate. We collected data in two configurations – one with parallel and one with perpendicular incident and outgoing light polarization. The probe beam was centered at 900 nm (1.38 eV) and was shone normal to the ab -plane with a 40 μm spot size. The pump beam was centered at 1030 nm (1.20 eV) and was incident at 15° to the surface normal with a 200 μm spot size. When the system is pumped with the laser pulse, the excited electrons remain within the t_{2g} manifold of the Ru $^{4+}$ atoms (the crystal field splitting to the e_g levels is ~ 2 eV) [41].

In the equilibrium state, the leading-order electric-dipole (ED) SHG contribution is allowed in CRO due to broken inversion symmetry (Fig. 1). At all temperatures, we obtain a good simultaneous fit to the parallel and perpendicular polarization configurations of the rotational anisotropy (RA) pattern with the ED contribution of the known point group symmetry C_{2v} [42] (Fig. 1(a)). In Fig. 1(c), we show the temperature dependence of the SHG intensity, $I^{2\omega}$, arising from the tensor element χ_{baa}^{ED} (red dot in Fig. 1(a)) across the insulator-metal transition. Although there is no temperature-induced change in symmetry of the RA pattern across the insulator-metal transition (Fig. 2(a)), the intensity exhibits a pronounced jump. (The offset between the reported value for $T_{MI}=48$ K and the observed jump around 46 K arises due to laser heating) [42]. No thermal hysteresis is measured, and no features are observed at T_N (Fig.1(c) inset).

Because the crystal, electronic and magnetic structure all change at T_{MI} , the cause of the observed jump in $I^{2\omega}$ is not immediately clear. A previous study reports a similar increase in $I^{2\omega}$ for pure CRO, but observes no such feature in the Fe-doped compound $\text{Ca}_3\text{Ru}_{1.95}\text{Fe}_{0.05}\text{O}_7$ [43]. This difference is striking because, similar to pure CRO, the latter compound undergoes a transition in which the spins reorient from pointing along the $\pm a$ axis to the $\pm b$ axis and a concomitant metal-insulator transition. However, unlike in pure CRO, this transition is not accompanied by a large structural change [37, 44]. We therefore conclude that the increase in $I^{2\omega}$ is indicative of the structural change (note that this is consistent with no features being observed at T_N Fig. 1(c)). To corroborate the connection between crystal structure and $I^{2\omega}$, in the Supplemental Material we use a Landau theory approach to show that a first-order transition with a symmetry-preserving order parameter can give rise to a jump in $I^{2\omega}$ [42].

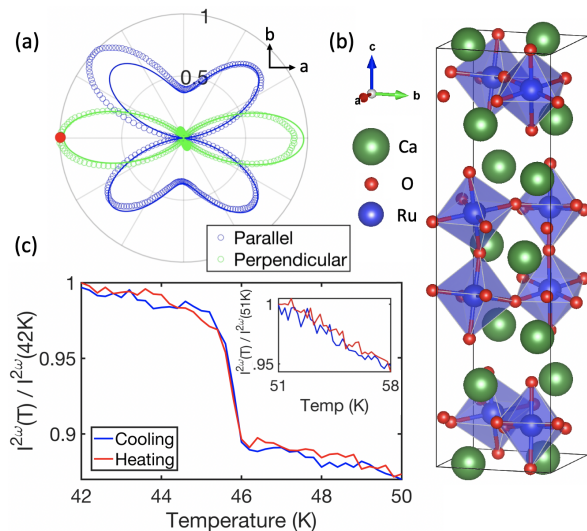


FIG. 1. (a) Measured RA-SHG patterns at 52 K with incident and outgoing polarizers in parallel and perpendicular geometry. Simultaneous fits to both channels are obtained using a susceptibility tensor constrained by the C_{2v} point group (solid lines). The data are normalized to a maximum in the perpendicular channel. The a and b crystallographic axes are indicated with black arrows. (b) Schematic of the low-temperature crystal structure. (c) Temperature dependence of the SHG intensity $I^{2\omega}$ at a polarization angle indicated by the red dot in (a). In this geometry, $I^{2\omega} \propto |\chi_{baa}^{ED}|^2$. The red(blue) curve corresponds to heating(cooling). (Inset) Normalized $I^{2\omega} \propto |\chi_{baa}^{ED}|^2$ across T_N .

We now study the PIPT instigated by intense femtosecond laser pulses. Figure 2(a) shows the change in the RA-SHG pattern above and below T_{MI} after the arrival of a 0.28 mJ/cm 2 pump pulse. Below T_{MI} , there is a clear drop in intensity following the pulse, while the pattern above T_{MI} is minimally affected. As in the thermal transition, the symmetry is unchanged. Figure 2(b) shows the evolution of $I^{2\omega} \propto |\chi_{baa}^{ED}|^2$ after photo-excitation at several temperatures. These curves demonstrate that the decrease in intensity is stable for $\gg 5$ ps. The magnitude of the drop in $I^{2\omega}$ is roughly constant for various temperatures below T_{MI} , but is markedly smaller in the high-temperature phase. (Here the measured T_{MI} is between 44-45 K due to laser heating from both pump and probe pulses). It should be noted that the intensity of the second harmonic, $I^{2\omega}$, varies across the sample surface (the ab plane) due to the nonuniform distribution of 180° polar domains, as discussed more thoroughly in Refs. [42, 45]. However, the photo-induced changes are associated only with the phase transition [42].

To understand the kinetics of the PIPT, we measure SHG time traces in the low temperature state for various pump fluences (Fig. 3(a)). We fit each time trace to the phenomenological function [42]:

$$u(t) = 1 + \left[\theta(t - t_0) I_\infty (1 - \alpha e^{-(t-t_0)/\tau}) \right] * g(w_0, t), \quad (1)$$

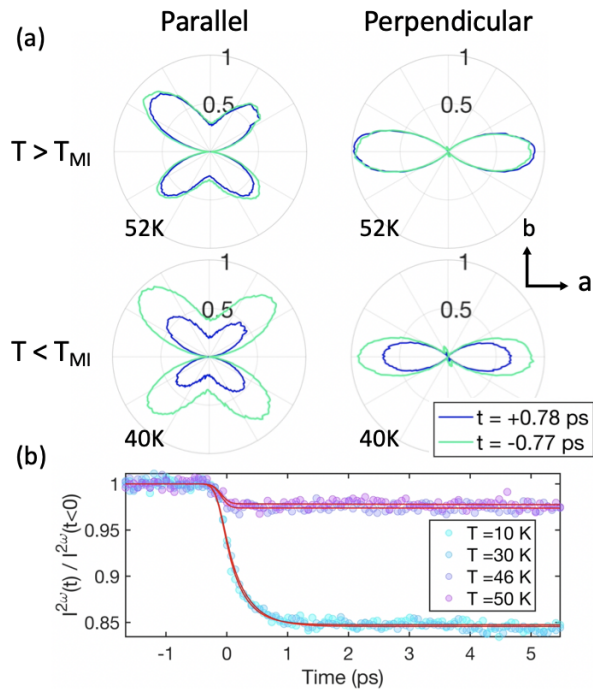


FIG. 2. Temperature-dependent SHG response to the 1030 nm pump pulse. (a) Rotational anisotropy patterns measured before ($t < 0$) and after ($t > 0$) a 0.28 mJ/cm^2 pump pulse both above and below T_{MI} . The pulse induces a large drop in SHG intensity when applied below T_{MI} and has little effect above T_{MI} . (b) Time traces of the normalized SHG intensity $I^{2\omega} \propto |\chi_{baa}^{ED}|^2$ at several temperatures with a 0.86 mJ/cm^2 pulse. Red lines are fits to Eq. (1). Traces at additional temperatures are excluded here for clarity and are presented in the Supplemental Material [42].

where $\theta(t)$ denotes the Heaviside step function, $g(w_0, t)$ is the cross-correlation of the pump and probe pulses and the $*$ indicates convolution. This allows us to extract three parameters: (i) the time constant of the transient decay, τ ; (ii) the SHG intensity at late times relative to the intensity before the pulse, I_∞ ; and (iii) the fraction of I_∞ that is related to the dynamics associated with τ , α . The best-fit values for τ , I_∞ , and αI_∞ are plotted as a function of fluence in Fig. 3(b). We find that I_∞ decreases with increasing fluence until reaching a saturation $I_\infty^{sat} \approx -0.11$ at fluence $F_{sat} \approx 0.4 \text{ mJ/cm}^2$, while αI_∞ decreases from zero to roughly half of I_∞^{sat} near F_{sat} before increasing at high fluence. The time constant τ exhibits the most noteworthy behavior; it first increases by nearly an order of magnitude from < 200 fs to ~ 1.4 ps, peaking near F_{sat} before decreasing to roughly 200 fs.

For fluences $F \gtrsim F_{sat}$, these measurements suggest that the sample has reverted to the high-temperature structure; the intensity jump observed as a function of temperature (Fig. 1(c)) is completely suppressed by the photo-exciting laser pulse. However, the nature of the “intermediate” states, characterized by $0 < |I_\infty| < |I_\infty^{sat}|$ is not immediately obvious. There are two natural pos-

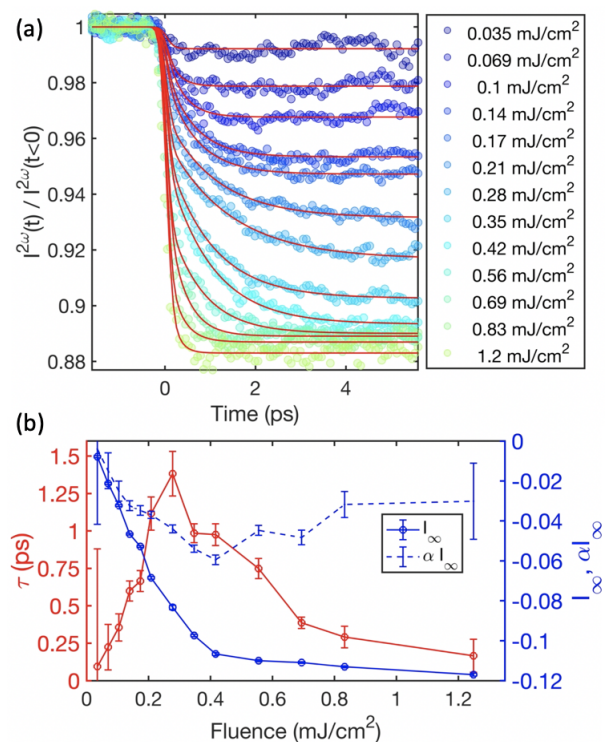


FIG. 3. (a) Time evolution of the normalized SHG intensity, $I^{2\omega} \propto |\chi_{baa}^{ED}|^2$, for varying pump fluences, measured at a nominal temperature of 4 K (laser heating raises the temperature). Fits to Eq. (1) are overlaid in red. (b) Best-fit values of I_∞ , αI_∞ , and τ plotted vs. pump fluence. Error bars are 95% confidence intervals from the fitting procedure.

sible scenarios to attribute to these states. In the first scenario, the lattice parameters would change in a spatially uniform manner throughout the illuminated region and would take on a value between that of the low- and high-temperature equilibrium phases. Alternatively, the effect of the pulse could be spatially nonuniform and the intermediate states could consist of small regions in which the lattice parameters primarily take on either their low- or high-temperature equilibrium values.

For several reasons, including the discontinuous character of the equilibrium transition and the observation of structural inhomogeneity in the hysteresis region of Ti-substituted CRO [46, 47], we expect *a priori* that the lattice parameters exhibit discontinuous changes. We show below that this scenario accounts for the experimental observations, most notably the non-monotonic fluence-dependence of the timescale τ (Fig. 3(b)).

To demonstrate that binary values of the lattice parameters can give rise to this behavior, we perform a bootstrap percolation simulation. The simulation consists of the following recipe [48]. (In the following, for ease of presentation, we refer only to the c -axis changes, but this is meant to represent the changes to all lattice parameters.) (1) An array of sites is defined that can

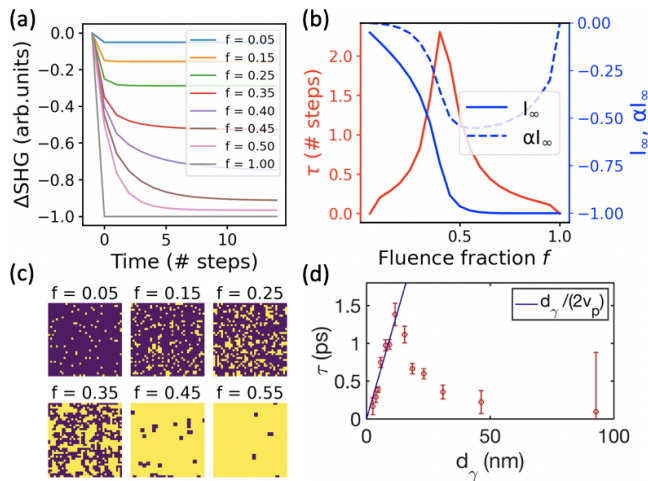


FIG. 4. (a) Simulated temporal evolution of SHG intensity for various fluence fractions f with strain threshold $\sigma_{th}=3$. ΔSHG is determined from the fraction of sites in the L_c state. Time steps indicate iterations of the simulation. (When compared to the experiment, each time step corresponds to a few hundred fs.) (b) The parameters τ , I_∞ , and αI_∞ determined from the simulations plotted against the fluence fraction parameter f . (c) Examples of two-dimensional slices of the final system state for various fluence fractions f . L_c (S_c) sites are depicted in yellow (purple). We estimate that each site corresponds to a region of the material with a length scale on the order of 1 nm [42]. (d) τ plotted versus the average distance between absorbed pump photons d_γ . The linear fit to the data in the high-fluence regime allows us to extract an approximate percolation speed v_p .

take only a long or short c -axis lattice parameter, denoted L_c and S_c , respectively. Before $t = 0$ the system is initialized to possess only S_c sites, corresponding to the low-temperature insulating state. (2) At $t = 0$, a random subset of sites is switched to the L_c state to mimic the effect of the pump. The number of switched sites is assumed to be proportional to the incident pump fluence. (3) Each remaining S_c site then evolves according to the governing rule that if the number of nearest neighbor L_c sites *exceeds* a threshold value, σ_{th} , the examined site switches from S_c to L_c . (4) Lastly, once converted to an L_c site, it is forbidden from reverting to an S_c one. These rules encompass the entire simulation, and it is run in discrete time steps until the system reaches quasi-equilibrium where site-switching no longer occurs. Imposition of the rule (4) is motivated by data showing that the recovery to the state with a globally contracted c -axis occurs on much longer timescales [42]. Because we disallow L_c -to- S_c conversion, the model describes a manifestly non-equilibrium process characterized by a breakdown of detailed balance and a transition to an absorbing state. With this minimal model taking a single input parameter, σ_{th} , we are able to capture the qualitative behavior of all three fitted parameters in our data.

In our implementation, the sample is modeled as a

$40 \times 40 \times 40$ cubic array of sites. The fraction of sites that are excited at $t=0$ is given by the fluence fraction parameter f , which is defined between 0 and 1, corresponding, respectively, to no pump pulse and to a pulse that excites all of the sites quasi-instantaneously. At each time step, the “strain” at each site, σ , is equal to the number of neighboring sites in the L_c state [42]. In the results of the simulation shown in Fig. 4, the threshold parameter, σ_{th} , is equal to three. To correlate the simulation to our data, we make the assumption that the change in $I^{2\omega}$ at each time step is proportional to the fraction of sites that have switched to the L_c state. This correspondence allows us to produce the simulated time traces in Fig. 4(a). Finally, we fit the simulated time traces to Eq. (1) (without the finite pulse width factor $g(w_0, t)$) to extract I_∞ , α , and τ as a function of the fluence fraction f (Fig. 4(b)) [42].

Figure 4 shows that this model reproduces all of the qualitative aspects of the SHG response. We emphasize that these simulations did not require fine-tuning to produce the desired results. Rather, we find that the non-monotonic fluence dependences of τ and of α , with peaks near F_{sat} , are robust to changes of σ_{th} and to the inclusion of additional neighbor couplings, both when the simulation is confined to two dimensions and when the penetration depths of the pump and probe pulses are taken into account. See the Supplemental Material [42] for details of the simulations using alternate settings.

We are left with the following physical picture to explain the non-monotonic behavior of the timescale τ . At low fluences, random isolated sites are photo-excited to the L_c state, but these sites cannot percolate very far; the S_c sites do not possess a sufficient number of L_c nearest neighbors to trigger a switching event. The observed transition time is therefore on the order of the exciting laser pulse in the experiment. As the fluence is increased, some sites that remained in the S_c state after the initial photo-excitation exceed the nearest neighbor strain threshold and turn into an L_c site. The L_c sites then start to percolate; switching events are able to trigger further switching events. Near the percolation threshold, where almost all the sites are switched, the transition time starts to lengthen considerably, mimicking critical slowing down [49]. At higher fluences, the number of sites that switch to the L_c state instantaneously is large and only a short time is needed to switch the remaining S_c sites. Within this framework, the peak in τ physically represents the maximum time it takes for the L_c site percolation to occur following the initial photo-excitation.

This physical picture also lends itself to a natural interpretation of the parameters I_∞ and α . In this scheme, I_∞ represents the total number of switched sites, including both the quasi-instantaneous effects from photo-excitation and the subsequent percolation. On the other hand, α describes the fraction of sites that convert from S_c to L_c solely due to percolation, and its dynamics are

associated with the timescale τ . The dip in αI_∞ with varying fluence thus indicates that the volume of the sample induced to become L_c through site-to-site spreading is largest at fluences near F_{sat} , in accordance to what would be expected near a percolation threshold (Fig. 4(b)). The interpretation of these parameters allows us to understand the PIPT as a percolation phenomenon mediated by local interactions between neighboring sites.

A physical justification that the interactions are mediated by lattice strain is obtained by an estimate of the percolation speed v_p . We first convert the fluence to an average distance between absorbed pump photons d_γ [42]. For fluences $F > F_{sat}$, this quantity characterizes the length over which an average L_c region percolates. (This is not the case for $F < F_{sat}$ when S_c regions will persist between sites excited by photons). We find that τ is linearly proportional to d_γ in this high-fluence (low d_γ) regime, indicating that the percolation speed is independent of fluence. Performing a linear fit, we extract a characteristic growth speed of ~ 4400 m/s (Fig. 4(d)). Though the speed of sound has not been measured in $\text{Ca}_3\text{Ru}_2\text{O}_7$, this value is in accord with what would be expected if the growth of L_c clusters was given by ballistic strain propagation.

In summary, our study provides substantial evidence that the kinetics of the PIPT in $\text{Ca}_3\text{Ru}_2\text{O}_7$ proceeds through the percolation of nanoscale clusters which is mediated by lattice strain. Specifically, the transition dynamics are qualitatively captured by a model of bootstrap percolation. The simplicity of this model suggests that it may hold significant promise for understanding the dynamics of other PIPTs. Indeed, time-resolved measurements of the photo-induced transition in VO_2 [18, 21, 50, 51] shows two timescales of comparable duration to those observed in this work, which may also be described within a percolation theory. Our work paves the way towards understanding the effects of dynamic inhomogeneity on PIPTs and provides a general model that may be useful for investigating photo-excited materials more broadly.

We thank R. Schonmann for helpful discussions regarding the percolation model, M. Rasiah for help with the initial construction of the second harmonic generation setup, and S. Kivelson for helpful suggestions regarding the Landau theory calculation. Research at UCLA was supported by the U.S. Department of Energy (DOE), Office of Science, Office of Basic Energy Sciences under Award No. DE-SC0023017 (experiment and simulations). Work at UC Boulder was supported by the National Science Foundation via Grant No. DMR 2204811 (materials synthesis). A.Z. acknowledges support by the Miller Institute for Basic Research in Science. A.K., R.A. and C.J.A. acknowledge the REU program through STROBE: a National Science Foundation Science and Technology Center under award no. DMR-1548924.

* tcarbin@g.ucla.edu

† anshulkogor@physics.ucla.edu

- [1] L. Stojchevska, I. Vaskivskiy, T. Mertelj, P. Kusar, D. Svetin, S. Brazovskii, and D. Mihailovic, *Science* **344**, 177 (2014).
- [2] J. Zhang, X. Tan, M. Liu, S. W. Teitelbaum, K. W. Post, F. Jin, K. A. Nelson, D. N. Basov, W. Wu, and R. D. Averitt, *Nature Materials* **15**, 956 (2016).
- [3] M. Mitrano, A. Cantaluppi, D. Nicoletti, S. Kaiser, A. Perucchi, S. Lupi, P. Di Pietro, D. Pontiroli, M. Riccò, S. R. Clark, D. Jaksch, and A. Cavalleri, *Nature* **530**, 461 (2016).
- [4] D. Fausti, R. I. Tobey, N. Dean, S. Kaiser, A. Dienst, M. C. Hoffmann, S. Pyon, T. Takayama, H. Takagi, and A. Cavalleri, *Science* **331**, 189 (2011).
- [5] A. Kogar, A. Zong, P. E. Dolgirev, X. Shen, J. Straquadine, Y.-Q. Bie, X. Wang, T. Rohwer, I.-C. Tung, Y. Yang, R. Li, J. Yang, S. Weathersby, S. Park, M. E. Kozina, E. J. Sie, H. Wen, P. Jarillo-Herrero, I. R. Fisher, X. Wang, and N. Gedik, *Nature Physics* **16**, 159 (2020).
- [6] J. W. McIver, B. Schulte, F.-U. Stein, T. Matsuyama, G. Jotzu, G. Meier, and A. Cavalleri, *Nature Physics* **16**, 38 (2020).
- [7] D. Perez-Salinas, A. S. Johnson, D. Prabhakaran, and S. Wall, *Nature Communications* **13** (2022).
- [8] D. Mihailovic and V. V. Kabanov, “Dynamic inhomogeneity, pairing and superconductivity in cuprates,” in *Superconductivity in Complex Systems: -/-*, edited by K. A. Müller and A. Bussmann-Holder (Springer Berlin Heidelberg, Berlin, Heidelberg, 2005) pp. 331–364.
- [9] E. Abreu, S. Wang, J. G. Ramírez, M. Liu, J. Zhang, K. Geng, I. K. Schuller, and R. D. Averitt, *Phys. Rev. B* **92**, 085130 (2015).
- [10] W. S. Lee, Y. D. Chuang, R. G. Moore, Y. Zhu, L. Patthey, M. Trigo, D. H. Lu, P. S. Kirchmann, O. Krupin, M. Yi, M. Langner, N. Huse, J. S. Robinson, Y. Chen, S. Y. Zhou, G. Coslovich, B. Huber, D. A. Reis, R. A. Kaindl, R. W. Schoenlein, D. Doering, P. Denes, W. F. Schlotter, J. J. Turner, S. L. Johnson, M. Först, T. Sasagawa, Y. F. Kung, A. P. Sorini, A. F. Kemper, B. Moritz, T. P. Devereaux, D.-H. Lee, Z. X. Shen, and Z. Hussain, *Nature Communications* **3**, 838 (2012).
- [11] E. Abreu, D. Meyers, V. K. Thorsmølle, J. Zhang, X. Liu, K. Geng, J. Chakhalian, and R. D. Averitt, *Nano Lett.* **20**, 7422 (2020).
- [12] S. Wall, S. Yang, M. Kozina, T. Katayama, T. Henighan, M. Trigo, O. Delaire, L. A. Boatner, D. A. Reis, T. A. Miller, M. Jiang, J. M. Glowina, M. Chollet, and L. Vidas, *Science* **362**, 572 (2018).
- [13] A. J. Sternbach, F. L. Ruta, Y. Shi, T. Slusar, J. Schalch, G. Duan, A. S. McLeod, X. Zhang, M. Liu, A. J. Millis, H.-T. Kim, L.-Q. Chen, R. D. Averitt, and D. N. Basov, *Nano Letters* **21**, 9052 (2021).
- [14] A. S. Johnson, D. Perez-Salinas, K. M. Siddiqui, S. Kim, S. Choi, K. Volckaert, P. E. Majchrzak, S. Ulstrup, N. Agarwal, K. Hallman, R. F. Haglund, C. M. Günther, B. Pfau, S. Eisebitt, D. Backes, F. Maccherozzi, A. Fitzpatrick, S. S. Dhesi, P. Gargiani, M. Valvidares, N. Artrith, F. de Groot, H. Choi, D. Jang, A. Katoch, S. Kwon, S. H. Park, H. Kim, and S. E. Wall, *Nature Physics* (2022).

- [15] B. T. O’Callahan, A. C. Jones, J. Hyung Park, D. H. Cobden, J. M. Atkin, and M. B. Raschke, *Nature Communications* **6**, 6849 (2015).
- [16] S. A. Dönges, O. Khatib, B. T. O’Callahan, J. M. Atkin, J. H. Park, D. Cobden, and M. B. Raschke, *Nano Letters* **16**, 3029 (2016).
- [17] D. J. Hilton, R. P. Prasankumar, S. Fourmaux, A. Cavalleri, D. Brassard, M. A. El Khakani, J. C. Kieffer, A. J. Taylor, and R. D. Averitt, *Phys. Rev. Lett.* **99**, 226401 (2007).
- [18] M. R. Otto, L. P. R. de Cotret, D. A. Valverde-Chavez, K. L. Tiwari, N. Émond, M. Chaker, D. G. Cooke, and B. J. Siwick, *PNAS* **116**, 450 (2019).
- [19] S. E. Madaras, J. A. Creeden, D. J. Lahneman, A. Harbick, D. B. Beringer, M. M. Qazilbash, I. Novikova, and R. A. Lukaszew, *Opt. Mater. Express* **10**, 1393 (2020).
- [20] M. Rodriguez-Vega, M. T. Simons, E. Radue, S. Kittiwatanakul, J. Lu, S. A. Wolf, R. A. Lukaszew, I. Novikova, and E. Rossi, *Phys. Rev. B* **92**, 115420 (2015).
- [21] T. L. Cocker, L. V. Titova, S. Fourmaux, G. Holloway, H.-C. Bandulet, D. Brassard, J.-C. Kieffer, M. A. El Khakani, and F. A. Hegmann, *Phys. Rev. B* **85**, 155120 (2012).
- [22] K. Haupt, M. Eichberger, N. Erasmus, A. Rohwer, J. Demsar, K. Rossnagel, and H. Schwoerer, *Phys. Rev. Lett.* **116**, 016402 (2016).
- [23] C. Laulhé, T. Huber, G. Lantz, A. Ferrer, S. O. Mariager, S. Grübel, J. Rittmann, J. A. Johnson, V. Esposito, A. Lübcke, L. Huber, M. Kubli, M. Savoini, V. L. R. Jacques, L. Cario, B. Corraze, E. Janod, G. Ingold, P. Beaud, S. L. Johnson, and S. Ravy, *Phys. Rev. Lett.* **118**, 247401 (2017).
- [24] T. Danz, T. Domröse, and C. Ropers, *Science* **371**, 371 (2021).
- [25] A. Zong, A. Kogar, Y.-Q. Bie, T. Rohwer, C. Lee, E. Baldini, E. Ergeçen, M. B. Yilmaz, B. Freelon, E. J. Sie, H. Zhou, J. Straquadine, P. Walmsley, P. E. Dolgirev, A. V. Rozhkov, I. R. Fisher, P. Jarillo-Herrero, B. V. Fine, and N. Gedik, *Nature Physics* **15**, 27 (2019).
- [26] D. Cho, S. Cheon, K.-S. Kim, S.-H. Lee, Y.-H. Cho, S.-W. Cheong, and H. W. Yeom, *Nature Communications* **7**, 10453 (2016).
- [27] L. Ma, C. Ye, Y. Yu, X. Lu, X. Niu, S. Kim, D. Feng, D. Tománek, Y.-W. Son, X. Chen, and Y. Zhang, *Nature Communications* **7**, 10956 (2016).
- [28] A. S. McLeod, J. Zhang, M. Q. Gu, F. Jin, G. Zhang, K. W. Post, X. G. Zhao, A. J. Millis, W. B. Wu, J. M. Rondinelli, R. D. Averitt, and D. N. Basov, *Nature Materials* **19**, 397 (2020).
- [29] Y. Yoshida, S.-I. Ikeda, H. Matsuhata, N. Shirakawa, C. H. Lee, and S. Katano, *Phys. Rev. B* **72**, 054412 (2005).
- [30] W. Bao, Z. Q. Mao, Z. Qu, and J. W. Lynn, *Phys. Rev. Lett.* **100**, 247203 (2008).
- [31] I. Marković, M. D. Watson, O. J. Clark, F. Mazzola, E. A. Morales, C. A. Hooley, H. Rosner, C. M. Polley, T. Balasubramanian, S. Mukherjee, N. Kikugawa, D. A. Sokolov, A. P. Mackenzie, and P. D. C. King, *PNAS* **117**, 15524 (2020).
- [32] M. Horio, Q. Wang, V. Granata, K. P. Kramer, Y. Sassa, S. Jöhr, D. Sutter, A. Bold, L. Das, Y. Xu, R. Frison, R. Fittipaldi, T. K. Kim, C. Cacho, J. E. Rault, P. L. Fèvre, F. Bertran, N. C. Plumb, M. Shi, A. Vecchione, M. H. Fischer, and J. Chang, *npj Quantum Materials* **6**, 29 (2021).
- [33] F. Baumberger, N. J. C. Ingle, N. Kikugawa, M. A. Hosain, W. Meevasana, R. S. Perry, K. M. Shen, D. H. Lu, A. Damascelli, A. Rost, A. P. Mackenzie, Z. Hussain, and Z.-X. Shen, *Phys. Rev. Lett.* **96**, 107601 (2006).
- [34] G. Cao, S. McCall, J. E. Crow, and R. P. Guertin, *Phys. Rev. Lett.* **78**, 1751 (1997).
- [35] B. Bohnenbuck, I. Zegkinoglou, J. Stempffer, C. Schüßler-Langeheine, C. S. Nelson, P. Leininger, H.-H. Wu, E. Schierle, J. C. Lang, G. Srajer, S. I. Ikeda, Y. Yoshida, K. Iwata, S. Katano, N. Kikugawa, and B. Keimer, *Phys. Rev. B* **77**, 224412 (2008).
- [36] J. F. Karpus, R. Gupta, H. Barath, S. L. Cooper, and G. Cao, *Phys. Rev. Lett.* **93**, 167205 (2004).
- [37] J. Peng, M. Q. Gu, X. M. Gu, G. T. Zhou, X. Y. Gao, J. Y. Liu, W. F. Xu, G. Q. Liu, X. Ke, L. Zhang, H. Han, Z. Qu, D. W. Fu, H. L. Cai, F. M. Zhang, Z. Q. Mao, and X. S. Wu, *Phys. Rev. B* **96**, 205105 (2017).
- [38] F. Lechermann, Q. Han, and A. J. Millis, *Phys. Rev. Research* **2**, 033490 (2020).
- [39] D. Puggioni, M. Horio, J. Chang, and J. M. Rondinelli, *Phys. Rev. Res.* **2**, 023141 (2020).
- [40] M. Fiebig, V. V. Pavlov, and R. V. Pisarev, *J. Opt. Soc. Am. B* **1**, 96 (2005).
- [41] J. Bertinshaw, M. Krautloher, H. Suzuki, H. Takahashi, A. Ivanov, H. Yavaş, B. J. Kim, H. Gretarsson, and B. Keimer, *Phys. Rev. B* **103**, 085108 (2021).
- [42] See Supplemental Material at [url] for more data analysis, theoretical calculations, and simulation results which includes Refs. [52–66].
- [43] S. Lei, S. Chikara, D. Puggioni, J. Peng, M. Zhu, M. Gu, W. Zhao, Y. Wang, Y. Yuan, H. Akamatsu, M. H. W. Chan, X. Ke, Z. Mao, J. M. Rondinelli, M. Jaime, J. Singleton, F. Weickert, V. S. Zapf, and V. Gopalan, *Phys. Rev. B* **99**, 224411 (2019).
- [44] X. Ke, J. Peng, W. Tian, T. Hong, M. Zhu, and Z. Q. Mao, *Phys. Rev. B* **89**, 220407 (2014).
- [45] S. Lei, M. Gu, D. Puggioni, G. Stone, J. Peng, J. Ge, Y. Wang, B. Wang, Y. Yuan, K. Wang, Z. Mao, J. M. Rondinelli, and V. Gopalan, *Nano Lett.* **18**, 3088–3095 (2018).
- [46] A. S. McLeod, A. Wieteska, G. Chiriaco, B. Foutty, Y. Wang, Y. Yuan, F. Xue, V. Gopalan, L. Q. Chen, Z. Q. Mao, A. J. Millis, A. N. Pasupathy, and D. N. Basov, *npj Quantum Materials* **6** (2021).
- [47] K. S. Rabinovich, A. N. Yaresko, R. D. Dawson, M. J. Krautloher, Y. L. Mathis, B. Keimer, and A. V. Boris, (2022), 10.48550/arxiv.2206.05005.
- [48] J. Adler, *Physica A: Statistical Mechanics and its Applications* **171**, 453 (1991).
- [49] A. Zong, P. E. Dolgirev, A. Kogar, E. Ergeçen, M. B. Yilmaz, Y.-Q. Bie, T. Rohwer, I.-C. Tung, J. Straquadine, X. Wang, Y. Yang, X. Shen, R. Li, J. Yang, S. Park, M. C. Hoffmann, B. K. Ofori-Okai, M. E. Kozina, H. Wen, X. Wang, I. R. Fisher, P. Jarillo-Herrero, and N. Gedik, *Phys. Rev. Lett.* **123**, 097601 (2019).
- [50] S. Wall, L. Foglia, D. Wegkamp, K. Appavoo, J. Nag, R. F. Haglund, J. Stähler, and M. Wolf, *Phys. Rev. B* **87**, 115126 (2013).
- [51] H.-W. Liu, W.-H. Liu, Z.-J. Suo, Z. Wang, J.-W. Luo, S.-S. Li, and L.-W. Wang, *PNAS* **119** (2022).
- [52] J. S. Lee, S. J. Moon, B. J. Yang, J. Yu, U. Schade,

- Y. Yoshida, S.-I. Ikeda, and T. W. Noh, *Phys. Rev. Lett.* **98**, 097403 (2007).
- [53] R. H. Schonmann, *The Annals of Probability* **20**, 174 (1992).
- [54] J. Balogh, B. Bollobás, and R. Morris, *Ann. Probab.* **37**, 1329 (2009).
- [55] J. Balogh, B. Bollobás, H. Duminil-Copin, and R. Morris, *Trans Am Math Soc* **364**, 2667 (2012).
- [56] A. E. Holroyd, *Probability Theory and Related Fields* **125**, 195 (2003).
- [57] V. Varadarajan, S. Chikara, V. Durairaj, X. Lin, G. Cao, and J. Brill, *Solid State Communications* **141**, 402 (2007).
- [58] A. Y. Kuznetsov, V. P. Dmitriev, O. I. Bandilet, and H.-P. Weber, *Physical Review B* **68**, 064109 (2003).
- [59] G. Azzolina, R. Bertoni, C. Ecolivet, H. Tokoro, S.-i. Ohkoshi, and E. Collet, *Physical Review B* **102**, 134104 (2020).
- [60] M. C. Shapiro, P. Hlobil, A. T. Hristov, A. V. Maharaj, and I. R. Fisher, *Physical Review B* **92**, 235147 (2015).
- [61] P. S. Pershan, *Physical Review* **130**, 919 (1963).
- [62] D. Sa, Valentí, R., and C. Gros, *Eur. Phys. J. B* **14**, 301–305 (2000).
- [63] N. A. Benedek and C. J. Fennie, *Physical Review Letters* **106**, 107204 (2011).
- [64] A. B. Harris, *Physical Review B* **84**, 064116 (2011).
- [65] N. A. Benedek, A. T. Mulder, and C. J. Fennie, *Journal of Solid State Chemistry* **195**, 11 (2012).
- [66] E. A. Nowadnick and C. J. Fennie, *Physical Review B* **94**, 104105 (2016).

Supplementary Material to “Evidence for bootstrap percolation dynamics in a photoinduced phase transition”

Tyler Carbin,^{1,*} Xinshu Zhang,¹ Adrian B. Culver,^{1,2} Hengdi Zhao,³ Alfred Zong,^{4,5} Rishi Acharya,¹ Cecilia J. Abbamonte,¹ Rahul Roy,^{1,2} Gang Cao,³ and Anshul Kogar¹

¹*Department of Physics and Astronomy, UCLA, Los Angeles, CA 90095-1547*

²*Mani L. Bhaumik Institute for Theoretical Physics, Department of Physics and Astronomy, University of California Los Angeles, Los Angeles, CA 90095*

³*Department of Physics, University of Colorado at Boulder, Boulder, Colorado 80309, USA*

⁴*Department of Chemistry, University of California at Berkeley, Berkeley, CA, 94720, USA*

⁵*Materials Sciences Division, Lawrence Berkeley National Laboratory, Berkeley, CA, 94720, USA*

(Dated: May 10, 2023)

CONTENTS

I. Rotational-Anisotropy SHG fitting	1	D. Second approach: Time-averaged Landau free energy	14
A. Imperfect alignment	2	1. SHG in a toy model	14
B. Multiple Domains	2	2. SHG near the metal-insulator transition in CRO	16
II. SHG Wavelength Dependence	3	References	17
III. Time Trace Fits	3		
IV. Recovery time traces	4		
V. Estimates of Time Resolution	4		
VI. Calculation of d_γ	5		
VII. Penetration depth calculations	5		
VIII. Considerations of homogeneous mechanisms	5		
IX. Simulation length and time scales	6		
X. Calculation of “strain” in the simulations	6		
XI. Fits to simulated time traces	7		
XII. Robustness of Simulation results	7		
A. Varying σ_{th}	7		
B. 2d Simulations	7		
C. Next-nearest neighbors	8		
D. Penetration depth effects	8		
XIII. Simulated Cluster Properties	9		
XIV. Temperature Effects	9		
A. Transient pump-induced heating	9		
B. Temperature-dependent time traces	11		
XV. Landau theory for SHG near the metal-insulator transition	12		
A. Symmetry-preserving transition	12		
B. Symmetry-allowed components of the SHG susceptibility tensor	13		
C. First approach: direct expansion	14		

I. ROTATIONAL-ANISOTROPY SHG FITTING

The observed rotational anisotropy (RA) SHG pattern is dominated by the leading-order electric dipole (ED) contribution to the nonlinear susceptibility χ_{ijk}^{ED} , defined by:

$$P_i(2\omega) = \chi_{ijk}^{ED} E_j(\omega) E_k(\omega), \quad (S1)$$

where $E_i(\omega)$ is the incident electric field at frequency ω , $P_i(2\omega)$ is the induced polarization in the sample at frequency 2ω , and a summation over repeated spatial indices is implied. This contribution to the measured SHG is in general larger than the subleading magnetic-dipole and electric-quadrupole terms by a factor of the incident wavelength divided by the lattice spacing [1], which here is ≈ 500 .

In general, the nonlinear susceptibility tensor describing ED SHG, $\chi_{ijk}^{ED} \equiv \chi_{ijk}$, is a third-rank tensor with 27 elements. Requiring the tensor to be invariant under all symmetry operations of the crystallographic point group C_{2v} ($mm2$), enforcing the permutation symmetry of indices j and k , and taking the axis of inversion symmetry breaking to be the b axis (see Sec. XV B) leaves 5 independent non-vanishing tensor elements:

$$\begin{aligned} \chi_{cbc} &= \chi_{ccb}, \\ \chi_{aba} &= \chi_{aab}, \\ \chi_{bcc}, \\ \chi_{baa}, \\ \chi_{bbb}. \end{aligned} \quad (S2)$$

The intensity of the second harmonic is proportional to the norm squared of the dot product of $\mathbf{P}(2\omega)$ and

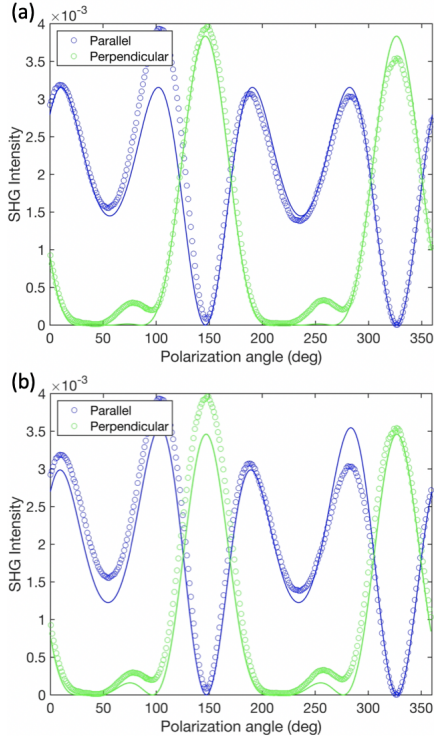


FIG. S1. RA-SHG data shown in Fig. 1(a) with (a) a fit to Eq. (S4) (this is the same as the polar plot in Fig. 1(a)) and (b) overlaid with a function given by (S5) with $\theta_a = \theta_c = 0.05$ rad.

the unit vector along the polarization direction of the analyzer $\mathbf{e}(2\omega)$:

$$I^{2\omega} \propto |\mathbf{e}(2\omega) \cdot \mathbf{P}(2\omega)|^2. \quad (\text{S3})$$

We then calculate the SHG intensity as a function of the polarization angle ϕ of the incident electric field for the cases in which the analyzer is either parallel or

perpendicular to the incident light polarization. In the normal-incidence geometry employed here, the incident electric field is restricted to the ab plane, so that all tensor elements with an index c do not appear in the expression for the SHG intensity. We find:

$$\begin{aligned} I_{Par}^{2\omega}(\phi) &\propto |\chi_{bbb}\cos^3\phi + (2\chi_{aba} + \chi_{baa})\cos\phi\sin^2\phi|^2 \\ I_{Perp}^{2\omega}(\phi) &\propto |\chi_{baa}\cos^3\phi + (\chi_{bbb} - 2\chi_{aba})\cos\phi\sin^2\phi|^2. \end{aligned} \quad (\text{S4})$$

These equations give the form of the fit shown in Fig. 1(a), where the tensor elements are simultaneously fit in the parallel and perpendicular channels. All time traces were measured with polarization angle $\phi = 0$ in the perpendicular channel such that $I^{2\omega} \propto |\chi_{baa}|^2$.

A. Imperfect alignment

The measured RA pattern contains small features that can not be captured by Equations S4. While these features are not relevant to the discussion in the main text, for completeness we show that they can be qualitatively captured by accounting for imperfections in the alignment of the crystal plane to the probe beam.

The effect of alignment imperfections on the RA-SHG pattern can be approximated by rotating the χ^{ED} tensor by small angles before calculating $I^{2\omega}(\phi)$. This significantly complicates the functional form of $I^{2\omega}$ and introduces terms containing elements χ_{ccb} and χ_{bcc} that are absent when the probe beam is exactly perpendicular to the ab plane of the crystal.

Figure S1(b) shows the RA data overlaid with a functional form given by Eq. S5 below. These functional forms account for tilts of the crystal about the a and c axes away from the ideal orientation in which the ab plane is exactly normal to the probe beam. Importantly, we find that the bumps in the perpendicular pattern at 80deg and 260deg can be qualitatively accounted for.

$$\begin{aligned} I_{Par}^{2\omega}(\phi) &\propto |(\cos\theta_c\cos\theta_a\cos\phi - \sin\theta_c\sin\phi)(\cos^2\phi((2\chi_{aba} + \chi_{baa})\cos^2\theta_a\sin^2\theta_c + (2\chi_{cbc} + \chi_{bcc})\sin^2\theta_a) + \\ &\quad (2\chi_{aba} + \chi_{baa} - \chi_{bbb})\cos\theta_a\sin(2\theta_c)\cos\phi\sin\phi + \chi_{bbb}\sin^2\theta_c + \cos^2\theta_c(\chi_{bbb}\cos^2\theta_a\cos^2\phi + (2\chi_{aba} + \chi_{baa})\sin^2\phi))|^2 \\ I_{Perp}^{2\omega}(\phi) &\propto \left| \frac{1}{2}(-\cos\theta_c(-2\chi_{aba} - \chi_{baa} - \chi_{bbb} + (2\chi_{aba} + \chi_{baa} - \chi_{bbb})\cos(2\theta_c))\cos^3\theta_a\cos^2\phi\sin\phi + \right. \\ &\quad \cos^2\theta_a\sin\theta_c\cos\phi((2\chi_{aba} - \chi_{baa} - \chi_{bbb} + (2\chi_{aba} + \chi_{baa} - \chi_{bbb})\cos(2\theta_c))\cos^2\phi - \\ &\quad 2(\chi_{baa} - \chi_{bbb} + (2\chi_{aba} + \chi_{baa} - \chi_{bbb})\cos(2\theta_c))\sin^2\phi) + \cos\theta_c\cos\theta_a\sin\phi((-2\chi_{cbc} - \chi_{bcc} - 2\chi_{baa} + 2\chi_{bbb} + \\ &\quad 2(2\chi_{aba} + \chi_{baa} - \chi_{bbb})\cos(2\theta_c) + (2\chi_{cbc} + \chi_{bcc})\cos(2\theta_a))\cos^2\phi - \\ &\quad (-2\chi_{aba} + \chi_{baa} + \chi_{bbb} + (2\chi_{aba} + \chi_{baa} - \chi_{bbb})\cos(2\theta_c))\sin^2\phi) + \cos\phi\theta_y(-2\chi_{bcc}\cos^2\phi\sin^2\theta_a - \\ &\quad \left. (-2\chi_{cbc} + 2\chi_{aba} + \chi_{baa} + \chi_{bbb} + (2\chi_{aba} + \chi_{baa} - \chi_{bbb})\cos(2\theta_c) + 2\chi_{cbc}\cos(2\theta_a))\sin^2\phi) \right|^2. \end{aligned} \quad (\text{S5})$$

B. Multiple Domains

If there are multiple domains in the probed region of the sample, the total SHG intensity at polarization angle

ϕ is given by

$$I_{tot}^{2\omega}(\phi) = \sum_i f_i I_i^{2\omega}(\phi), \quad (\text{S6})$$

where the sum is over unique domains and f_i gives the fraction of the probed region of the sample that constitutes the i^{th} domain.

By referring to Eq. (S4), we see that if there exist two domains related by $\phi \rightarrow \phi + 90^\circ$, then there exists no angle for which the total SHG intensity $I_{\text{tot}}^{2\omega}(\phi)$ is zero. Domains related by a 90° rotation of the polar moment therefore lift the nodes in the RA-SHG pattern and are not present in the data presented here.

On the other hand, the 180° polar domains can only change the magnitude of $I^{2\omega}$ as a function of position in the ab plane. This is discussed at length in Ref. [2]. Thus, one cannot reliably compare the magnitude of the pump-induced drop in $I^{2\omega}$ between data-sets (it varied between $\sim 4\text{-}40\%$ in our measurements, but was typically $\sim 15\%$). Nonetheless, at a single spot, the jump in $I^{2\omega}$ is constant, which indicates that the 180° domains are static upon photo-excitation and that the dominant dynamics are associated with the insulator-metal transition.

II. SHG WAVELENGTH DEPENDENCE

Figure S2(a) shows the dependence of the RA-SHG pattern on the wavelength of the probe beam between 820nm and 940nm. Fig. S2(b) shows the value of $\max(I^{2\omega}(\phi))$ in the two channels. The only change in the pattern comes from the dependence of the tensor elements on the light wavelength. The same fitting function Eq. S5 can be used to fit the RA-SHG pattern at each wavelength.

III. TIME TRACE FITS

All time traces are fit to Eq. 1 of the main text. For the data point at the largest fluence (1.2 mJ/cm^2), τ was restricted to be larger than 100 fs so that the fitting procedure would converge to a solution. Because the best-fit value of τ is found to be ≈ 170 fs (i.e. larger than this lower bound), we do not expect that this constraint significantly altered the extracted value. However, it is possible that this constraint resulted in an underestimation of the uncertainties of the extracted τ and α at this fluence.

There are two timescales in Eq. 1 that correspond to physical processes in the sample: τ and a shorter timescale represented by the Heaviside function that is smaller than, or comparable to our experimental time resolution ≈ 280 fs (c.f. Section V). Fig. S3 shows that the inclusion of only one of these timescales without the other is insufficient to obtain a good fit to the measured time traces and thus that the presence of both in Eq. 1 is necessitated by the data. The left panel of Fig. S3 shows that fits lacking a short timescale to govern the immediate drop in intensity after the pump pulse cannot capture

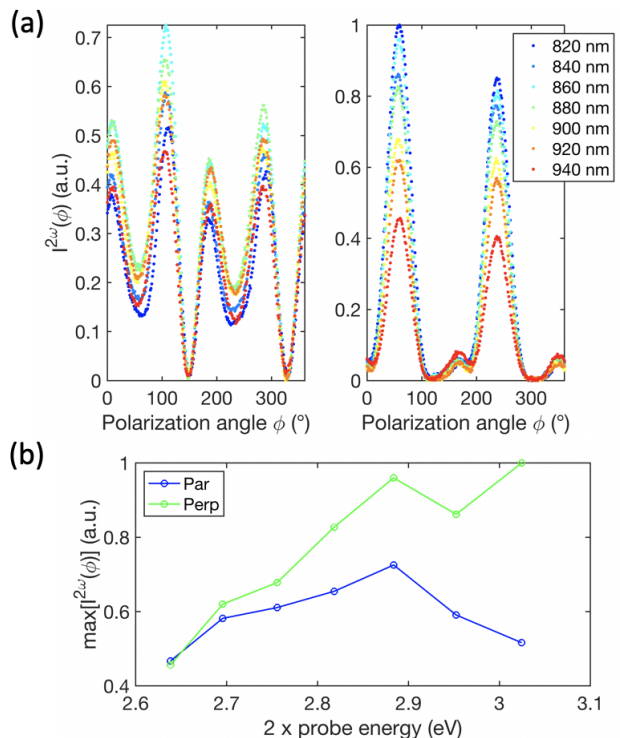


FIG. S2. (a) Wavelength dependence of the RA-SHG measurements in both parallel (left) and perpendicular (right) polarization channels. There is a 90° offset between the two channels. (b) The maximal value in the $I^{2\omega}$ curves from a plotted vs. twice the probe energy.

the data well. In particular, the fits shown are of the data after t_0 to a simple exponential decay with no convolution with the cross-correlation of the pump and probe pulses $g(w_0, t)$. Similarly, to demonstrate that the time constant τ is necessary to obtain a good fit, we present attempted fits to Eq. S7 in the second column of Fig. S3. This function has no exponential decay but includes an error function of variable width w that approximates the Heaviside function in the limit that $w \rightarrow 0$. Lastly, the third column displays attempted fits to Eq. 1 with α fixed to one. This demonstrates that, to obtain a satisfactory fit, the exponential term must have a different weight from the term that has only the Heaviside function.

$$u(t) = 1 + \left[\frac{1}{2} \left(1 + \text{Erf} \left(\frac{2\sqrt{\ln(2)}(t - t_0)}{w} \right) \right) I_\infty \right] * g(w_0, t). \quad (\text{S7})$$

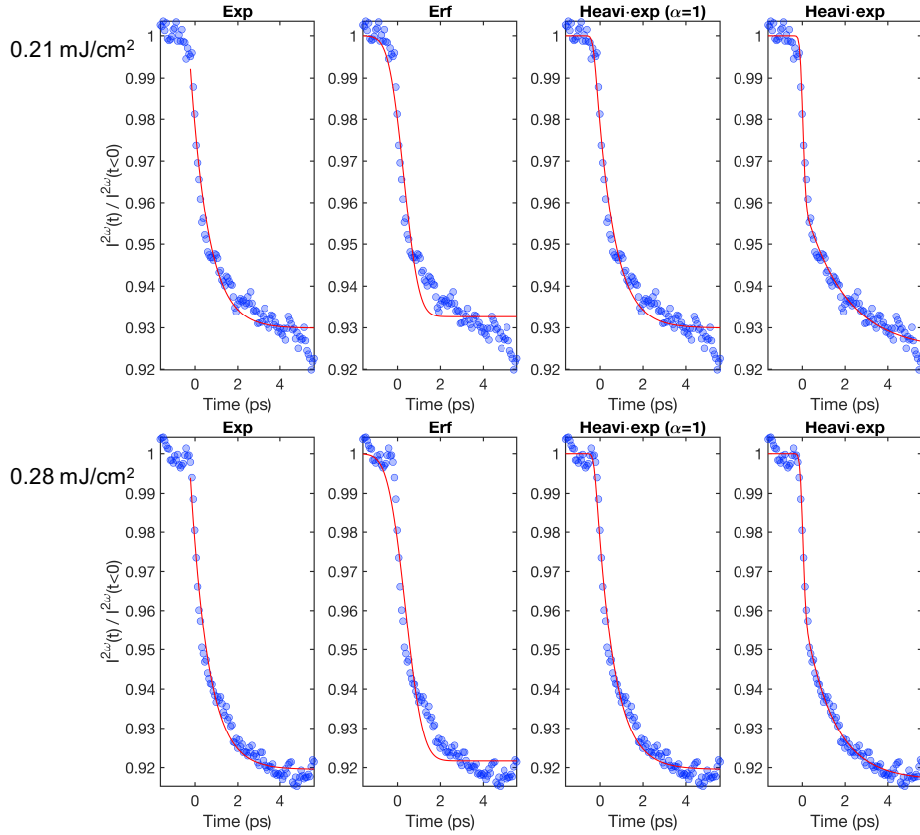


FIG. S3. Attempted fits to the 0.21 mJ/cm² (top) and 0.28 mJ/cm² (bottom) time traces shown in Fig. 3 using various fitting functions. The left column shows the attempted fit of all time points after t_0 to a simple exponential decay with variable decay constant. The second column shows attempted fits to an error function of variable width with a convolution of the pump-probe cross correlation. The third column shows the fits to Eq. 1 with α fixed to one. The right column shows the fits to Eq. 1 that are used in the main text.

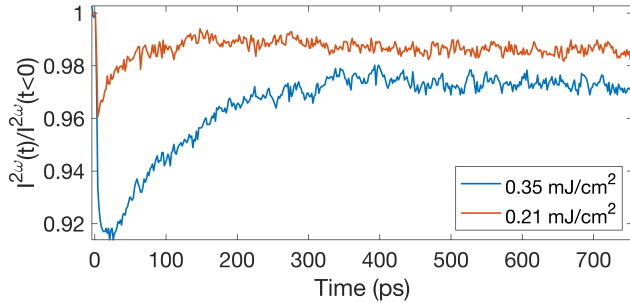


FIG. S4. SHG time traces taken over 100s of ps to show the recovery between pulses.

IV. RECOVERY TIME TRACES

Figure S4 shows the recovery of $I^{2\omega}$ following the pump pulse. These traces show that the recovery timescale (hundreds of ps) is much longer than the timescale for the initial insulator-metal transition, which justifies our separation of timescales in the percolation model.

V. ESTIMATES OF TIME RESOLUTION

In addition to the intrinsic widths of the pump and probe pulses, the time resolution of the experiment is affected by the angle mismatch between the two beams. In the limit in which both the pump and probe beams are normally incident on the sample, the cross-correlation between the two Gaussian profiles each with a $\sigma=77$ fs (181 fs FWHM) is another Gaussian with $\sigma=\sqrt{2}(77 \text{ fs}) = 109$ fs (256 fs FWHM). For the geometry employed in the experiment, we can obtain an upper bound on the time resolution by adding the time interval between the arrival of the pump pulse at the near and far ends of the transverse probe profile to the “intrinsic” width of the pump pulse. This correction gives: $\Delta t = \text{FWHM}_{\text{probe}} \sin(15^\circ)/c = 35$ fs. Thus, the obtained upper bound for the FWHM of the cross-correlation between the pump and probe pulses in the experiment is $\sqrt{(181)^2 + (181 + 35)^2}$ fs = 282 fs.

We can also estimate the experimental time resolution from the fitted time traces and compare it to this upper bound. To do this, we fit the derivative of the time trace

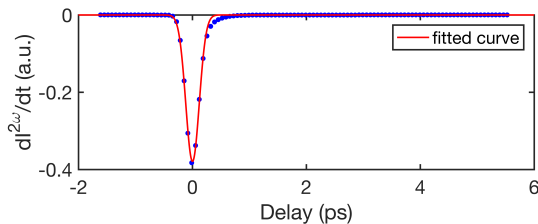


FIG. S5. The time-derivative of the fitted curve shown in Fig 3 in the main text for 1.2 mJ/cm^2 (blue points) and a gaussian fit (red) used to determine the experimental time resolution.

corresponding to the largest fluence (1.2 mJ/cm^2) to a gaussian. If we assume that the drop in SHG intensity occurs much faster than the time resolution of our experiment, the width of the fitted gaussian is a measure of our experimental time resolution. (Otherwise, it is an upper bound). The derivative of the fitted curve for the time trace corresponding to the largest fluence and the gaussian fit to this derivative are shown in Fig. S5. The experimental time resolution determined from this procedure is **278 fs** (given by the FWHM of the gaussian). This value is in remarkable agreement with the upper bound estimated above, 282 fs.

VI. CALCULATION OF d_γ

We use the following equations to calculate the number of photons absorbed by a single pulse and the number of unit cells impinged by a single pulse

$$N_\gamma = (1 - R)F \frac{1}{h\nu} \pi (\text{hwhm}_{pump})^2, \quad (\text{S8})$$

$$N_{u.c.} = \frac{\pi (\text{hwhm}_{pump})^2 \delta(\omega_{pump})}{abc}, \quad (\text{S9})$$

where R is the reflectivity of CRO at 1030 nm, $h\nu$ is the energy of a single 1030 nm photon, and $\delta_{pump} \approx 78 \text{ nm}$ is the penetration depth of the pump laser (c.f. Section VII). We find the number of unit cells per absorbed pump photon to be $N_{u.c.}/N_\gamma = 11.5$ at the largest τ .

We can then multiply by the average lattice parameter $\bar{a} \equiv \frac{a+b+c}{3} = 10.1 \text{ \AA}$ to obtain the average distance between absorbed pump photons d_γ :

$$d_\gamma \approx \frac{N_{u.c.} \bar{a}}{N_\gamma}. \quad (\text{S10})$$

VII. PENETRATION DEPTH CALCULATIONS

To determine the penetration depths of the pump laser (1030 nm) and of the first- (900 nm) and second-

(450 nm) harmonic probe beams, we performed reflectivity measurements of the sample at each of these wavelengths. To verify this method, we also measure the reflectivity at 800 nm for comparison with the penetration depth reported in Ref. [2]. We use these reflectivity measurements in conjunction with previous measurements [2] of the real part of the conductivity, σ_1 , to determine the penetration depths.

The reflectivity R is related to the optical conductivity by the following expression (in cgs units):

$$R = \frac{1 + \frac{4\pi}{\omega}(\sigma_1^2 + \sigma_2^2)^{1/2} - \left(\frac{8\pi}{\omega}\right)^{1/2} \left((\sigma_1^2 + \sigma_2^2)^{1/2} + \sigma_2 \right)^{1/2}}{1 + \frac{4\pi}{\omega}(\sigma_1^2 + \sigma_2^2)^{1/2} + \left(\frac{8\pi}{\omega}\right)^{1/2} \left((\sigma_1^2 + \sigma_2^2)^{1/2} + \sigma_2 \right)^{1/2}}, \quad (\text{S11})$$

where $\sigma_{1(2)}$ is the real(imaginary) part of the optical conductivity. From this, we extract $\sigma_2(\omega)$ at the desired frequencies, which we use to compute the penetration depth δ :

$$\delta = \frac{c}{(2\pi\omega)^{1/2}} \left((\sigma_1^2 + \sigma_2^2)^{1/2} + \sigma_2 \right)^{-1/2}, \quad (\text{S12})$$

where we have taken $\mu_1=1$.

The measured values of the reflectivity R_{meas} are included in Table I. Of the relevant wavelengths, only the reflectivity at 1030 nm has been previously measured [3], and the value reported here (0.18) is in good agreement with these prior results. However, for all included wavelengths, the measured reflectivity is inconsistent with the previously reported values for σ_1 . In particular, using the values for σ_1 in the literature and the measured reflectivity, Eq. S11 yields a complex value for σ_2 , which is defined to be real. This result is unphysical. Substituting larger values for the reflectivity, however, yields real values for σ_2 at all considered wavelengths. To determine the penetration depth, we use the minimum reflectivity (R_{det}) that results in a real-valued (and thus, physical) σ_2 . (In all cases, the difference with the measured reflectivity was less than or equal to 3%). This procedure is validated by the penetration depth calculated using this method at 800 nm (73 nm), which is in exact agreement with that reported in Ref. [2]. The calculated penetration depth at 450 nm is also similar to that reported at 400 nm [2]. The results of the penetration depth calculations are summarized in Table I.

VIII. CONSIDERATIONS OF HOMOGENEOUS MECHANISMS

In the main text we have argued for the existence of percolating inhomogeneity in the PIPT by correlating our measurements with simulations of inhomogeneous dynamics. While the possibility of a homogeneous PIPT mechanism cannot be excluded by these results, we argue here that such a scenario is unlikely. The most essential

λ (nm)	σ_1 (THz)	$R_{det}(R_{meas})$	σ_2 (THz)	δ (nm)
800	681	0.19(0.16)	373	73
450	1330	0.20	930	31
900	614	0.19(0.16)	365	76
1030	576	0.20(0.18)	576	78

TABLE I. The penetration depth δ in CRO at the pump wavelength 1030 nm, at the first- (900 nm) and second- (450 nm) harmonic probe wavelengths, and at 800 nm for comparison to Ref. [2]. The real and imaginary parts of the optical conductivity, and the measured and determined values for the reflectivity that are used to calculate the penetration depth are also included.

feature of our data that appears to require the invocation of spatial inhomogeneity is the non-monotonic fluence dependence of the time constant τ . If the PIPT is thought to be homogeneous, additional description is needed to explain this behavior.

One recent study [4] used a time-dependent Ginzburg-Landau formalism to describe the non-monotonic fluence dependence of the photo-induced transition time in a charge density wave compound. In this picture, the slowdown in τ appears due to fluctuations with correlation lengths that diverge near a critical fluence. One might suspect that a similar description applies here. However, the PIPT observed in CRO appears substantially different from the previous study in several respects.

First, in the previous study there is only one observed timescale governing the photoinduced transition due to the coherent displacive motion of the atoms. It is this timescale that exhibits the slowing down behavior. In comparison, there exist at least two timescales involved in the transition process measured in this work (Fig. S3). While the presence of two timescales is an essential feature of our inhomogeneous model (being associated with the quasi-instantaneous structural change associated with the absorption of light and with the subsequent percolation), there is no apparent analogue to the longer timescale in the homogeneous Ginzburg-Landau picture. Additionally, the change in the decay time constant observed in the previous work is much smaller (~ 300 - 400 fs) than that seen here, despite both transitions involving changes to the crystal lattice. This observation suggests that the coherent motion of atoms cannot explain the exponential part of the dynamics, which is consistent with mesoscale structural inhomogeneity in CRO. In summary, unlike a Ginzburg-Landau description, mesoscopic percolation in CRO offers a natural explanation for (1) why there exist two timescales in CRO and (2) why the timescale of the decay in CRO should be significantly longer than that in the previous study [4].

We have addressed the possibility of an explanation based on a time-dependent Ginzburg-Landau theory in

detail because it is, to our knowledge, the most straightforward way in which one might attempt to attribute our observations to homogeneous dynamics. There are surely other possibilities that we have not considered. However, we emphasize several reasons why the appearance of mesoscale inhomogeneity may be expected: (1) the well-documented appearance of inhomogeneity in the vicinity of first-order insulator-metal transitions, (2) the central role inhomogeneity plays in the observed colossal magnetoresistance effect, which is observed in CRO, (3) the observation of inhomogeneity in the Ti-doped compound [5], and (4) that the nearly binary nature of the c axis change observed in equilibrium is likely to persist away from equilibrium [6].

IX. SIMULATION LENGTH AND TIME SCALES

Although the simulations alone are devoid of any length/time scale, we can extract crude estimates for the physical scales that correspond to elements of the simulation by comparing the simulation output with the data. By equating the peak value of τ from the measurements with that from the simulation, we get that one time step in the simulation corresponds to several hundred fs. Using this value, and equating the percolation speed to the “percolation speed” of the simulations (1 site per time step), we find that the length scale corresponding to a single site in the simulation is on the order of 1 nm.

X. CALCULATION OF “STRAIN” IN THE SIMULATIONS

The “strain” in the simulations (that dictates a switch to the L_c state when greater than or equal to σ_{th}) is calculated according to the following equations:

$$\begin{aligned}
\sigma_{3D}(i, j, k) &= s_{i+1, j, k} + s_{i, j+1, k} + s_{i, j, k+1} + \dots \\
&\quad s_{i-1, j, k} + s_{i, j-1, k} + s_{i, j, k-1} + \dots \\
&\quad \beta(s_{i+1, j+1, k} + s_{i-1, j+1, k} + s_{i+1, j-1, k} + \dots \\
&\quad s_{i-1, j-1, k} + s_{i+1, j, k+1} + s_{i-1, j, k+1} + \dots \\
&\quad s_{i+1, j, k-1} + s_{i-1, j, k-1} + s_{i, j+1, k+1} + \dots \\
&\quad s_{i, j-1, k+1} + s_{i, j+1, k-1} + s_{i, j-1, k-1}), \\
\sigma_{2D}(i, j) &= s_{i, j+1} + s_{i, j-1} + s_{i+1, j} + s_{i-1, j} + \dots \\
&\quad \beta(s_{i+1, j+1} + s_{i-1, j+1} + s_{i-1, j-1} + s_{i-1, j-1}).
\end{aligned} \tag{S13}$$

where $\sigma_{2D}(\sigma_{3D})$ is used for a two-(three-)dimensional simulated sample. $s_{i, j, k} \in \{0, 1\}$ is the state of site (i, j, k) where 0 and 1 correspond to the L_c and S_c states, respectively. These equations also define the next-nearest neighbor coupling with a coupling strength given by the parameter $\beta \in [0, 1]$ (which is set to zero in the simulations

included in the main text).

XI. FITS TO SIMULATED TIME TRACES

The fits to the simulated time traces were performed with a procedure almost identical to the fitting of the experimental data. The only difference is the removal of the cross correlation factor, which accounts for the temporal resolution associated with the laser pulses. Fig. S6 shows fits of the simulated time traces to Eq. 1 of the main text excluding the cross-correlation term.

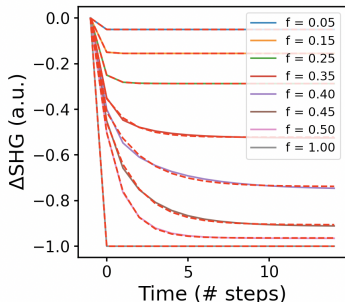


FIG. S6. Fits (dashed red curves) of simulated time traces shown in the main text to Eq. 1 without a convolution with the cross correlation factor.

XII. ROBUSTNESS OF SIMULATION RESULTS

Bootstrap percolation models have been widely studied in the mathematics literature. In the thermodynamic limit, the entire system becomes activated at a fraction of initialized sites p_c which approaches 0 or 1 depending on the dimension and the number of nearest neighbors required for activation [7]. However, finite-size effects are found to dominate the dynamics of even the largest computer simulations. Indeed the threshold of percolation has been found to approach the thermodynamic limit as slowly as $\frac{C}{\log(\log(n))}$ for a system of size n^3 in some of the models that we have studied here [8, 9]. Thus, the percolation process undergone during the PIPT studied here is almost certainly far from the thermodynamic limit, and is best studied via computer simulation.

In this section we show that variations of the simulation discussed in the main text produce time traces that preserve the salient qualitative features of the traces. In particular, the peak in the time constant τ as a function of fluence fraction f and its alignment with the saturation of I_∞ , as well as the f -dependence of αI_∞ that is non-monotonic and goes to zero at extremal values of f , are reproduced in the various simulations shown below. These features should therefore be understood as rather general consequences of our proposed model as opposed

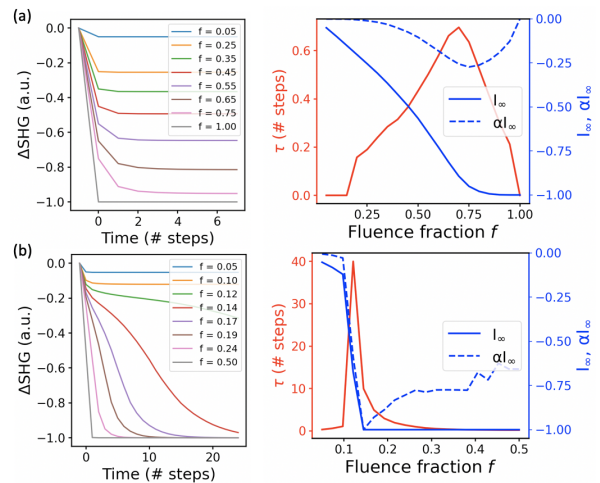


FIG. S7. Simulated time traces and extracted fit parameters with $\sigma_{th} = 4$ (top) and $\sigma_{th} = 2$ (bottom) (with $\beta = 0$). Note that the x -axes are not the same in the two cases.

to artifacts of the specific settings with which the simulation in the main text was performed.

A. Varying σ_{th}

Figure S7 shows the output of simulations using a $30 \times 30 \times 30$ array with σ_{th} changed from 3 as in the main text to 2 and to 4. (No significant differences were observed between simulations using a $30 \times 30 \times 30$ and a $40 \times 40 \times 40$ array.) As may be expected, the value of f at which τ peaks and I_∞ saturates increases with σ_{th} .

While the $\sigma_{th} = 4$ case retains time traces that appear similar to those in the data and in the $\sigma_{th} = 3$ case, the $\sigma_{th} = 2$ case appears qualitatively different. For the $\sigma_{th} = 2$ case and more generally for $\sigma_{th} < d$ where d is the dimension of the model, one expects a sharp transition for large enough systems based on rigorous results in the mathematics literature [8, 10]. Our simulations for higher values of σ_{th} seem to indicate the lack of a sharp transition at least at the system sizes that we have simulated. We take this as evidence that the experiment is best modeled with $\sigma_{th} = d$. Nonetheless, in all cases the general behavior of the three fit parameters is preserved.

B. 2d Simulations

The broad qualitative features of the simulated time traces are unchanged when the simulation is limited to two spatial dimensions. The results of the 2d simulation for $\sigma_{th}=2$ and $\beta=0$ are shown in Fig. S8.

Fig. S8 establishes that our model of percolating inhomogeneity reproduces the qualitative features observed in the experiment even if the simulation is confined to two dimensions.

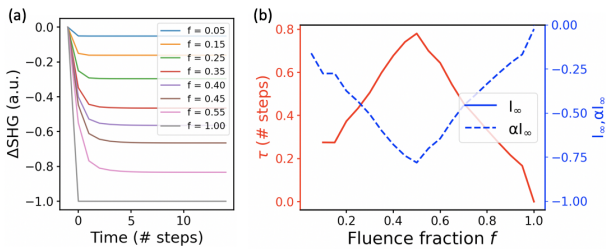


FIG. S8. Simulated SHG time traces (a) and extracted fit parameters (b) for a 2d 30x30 simulation with $\sigma_{th}=2$ and $\beta=0$.

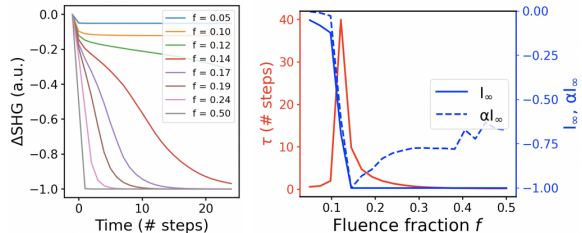


FIG. S9. Simulated time traces and extracted fit parameters for a 30x30x30 array with $\sigma_{th} = 3$ and $\beta = 0.1$.

C. Next-nearest neighbors

We introduce coupling between next-nearest neighbors by setting $\beta > 0$ in Eq. S13. Figure S9 shows the simulated time traces and extracted parameters for the 30x30x30 simulation with $\sigma_{th} = 3$ and $\beta = 0.1$. Again we find that, while the simulated time traces appear more complicated than the data, the f -dependence of the parameters is qualitatively unchanged.

One may be tempted to interpret this as indicative that the next-nearest neighbor coupling between sites is insignificant in the PIPT in CRO. However, by increasing both σ_{th} and β , one finds that there are many combinations of the two parameters (in both 2d and 3d) that appear to reproduce the qualitative features of the data. The results of several of these simulations are shown in Figures S10 and S11 for the 3d and 2d cases respectively.

D. Penetration depth effects

In principle, the finite penetration depths of the pump and probe lasers introduce another type of inhomogeneity into the PIPT. Namely, the number of (pump and probe) photons absorbed by the sample falls off exponentially as a function of the depth from the surface. In this section we demonstrate that the qualitative results of the simulations are preserved when this additional inhomogeneity is accounted for.

The intensity of the pump beam as a function of

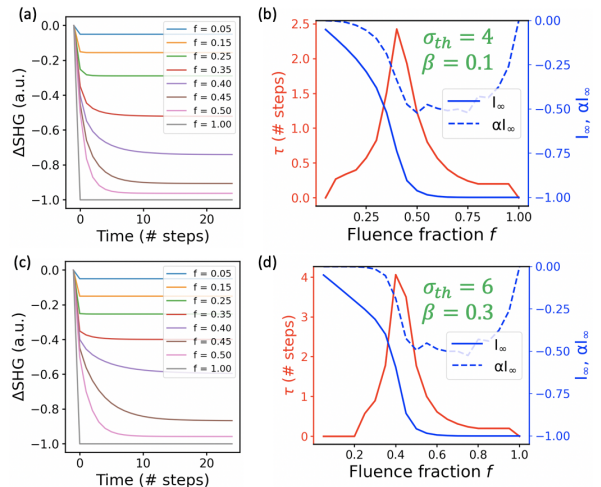


FIG. S10. Simulated time traces and extracted fit parameters for 3d 30x30x30 array simulations with (a)(b) $(\sigma_{th}, \beta)=(4, 0.1)$ and (c)(d) $(\sigma_{th}, \beta)=(6, 0.3)$

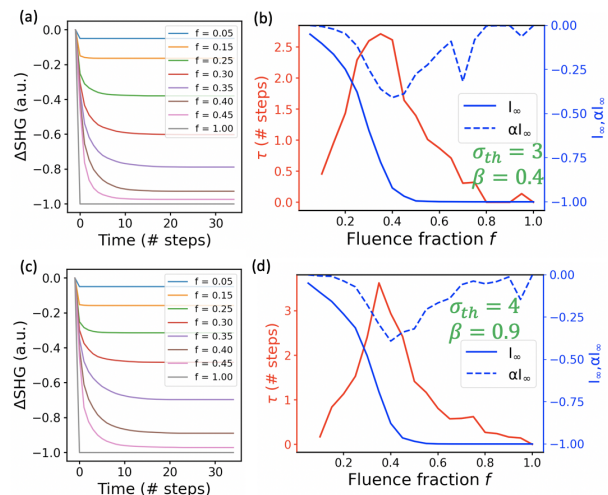


FIG. S11. Simulated time traces and extracted fit parameters for 2d 30x30 array simulations with (a)(b) $(\sigma_{th}, \beta)=(3, 0.4)$ and (c)(d) $(\sigma_{th}, \beta)=(4, 0.9)$

depth z falls off exponentially with the penetration depth $\delta(\omega_{pump})$:

$$I_{pump}(z) \propto e^{-z/\delta(\omega_{pump})}. \quad (\text{S14})$$

In the simulations, this effect is captured by scaling the probability of activating a site at $t = 0$ (given by the fluence fraction f) by this exponential factor, where z is now the discrete z -coordinate in the simulated array, and the penetration depth is an unknown number of array sites (discussed further below).

To account for the finite penetration depth of our SHG probe, we must consider both the penetration depth of the incident laser at frequency ω and that of the generated second harmonic 2ω . The second-harmonic field generated at a depth z is proportional to the square of

the field at position z with frequency ω , which decays exponentially with the penetration depth $\delta(\omega)$:

$$E^{2\omega}(z) \propto E^\omega(z)^2 \propto e^{-z/\delta(\omega)}. \quad (\text{S15})$$

The generated second harmonic intensity is then partially absorbed by the sample before returning to the surface. Thus, the light that contributes to the measured SHG intensity is additionally damped along the z direction due to the penetration depth of the second harmonic. This leads to an effective penetration depth of the SHG probe:

$$I_{\text{contr}}^{2\omega}(z) \propto e^{-z/\delta(2\omega)} e^{-z/\delta(\omega)} = e^{-z/\delta^{\text{eff}}}, \quad (\text{S16})$$

where we have defined the effective penetration depth:

$$\delta^{\text{eff}} \equiv \frac{\delta(\omega)\delta(2\omega)}{\delta(\omega) + \delta(2\omega)}. \quad (\text{S17})$$

To incorporate the effect of this finite-size penetration depth into the simulations, the simulated SHG intensity, which was previously simply proportional to the number of S_c sites, is now proportional to the number of S_c sites weighted by $e^{-z/\delta^{\text{eff}}}$, where z is the discrete z -coordinate in the array and δ^{eff} is an unknown number of array sites (discussed further below).

Using the values for the penetration depth at 900 nm and 450 nm in Table I, we obtain an effective probe penetration depth of ≈ 22 nm, which is ≈ 3.5 times smaller than the penetration depth of the pump beam, $\delta(\omega_{\text{pump}})$. This ratio being significantly greater than one helps to explain why simulations neglecting penetration depth effects agree well with experiment; the probe samples from a much smaller volume of the material than that which is excited by the pump pulse. Thus, in the region sampled by the probe, the inhomogeneity due to the penetration depth of the pump is a small effect.

In incorporating finite penetration depth effects into the simulations, the ratio $\delta(\omega_{\text{pump}})/\delta^{\text{eff}}$ must be preserved. However, we do not know the magnitude of the penetration depths that should be used in the simulations (in units of number of array sites) to obtain the closest correspondence to the physical experiment. Therefore, in Figure S12 we present the results of several simulations in which the magnitude of the penetration depths is varied while the ratio $\delta(\omega_{\text{pump}})/\delta^{\text{eff}} = 3.5$ is fixed. Simulation output corresponding to several different values of $\delta(\omega_{\text{pump}})$ are shown. We have estimated that each site in the simulations corresponds to a length on the order of ~ 1 nm in the experiment (c.f. Section IX). Thus, in Fig. S12(a) we present the simulation output with $\delta(\omega_{\text{pump}})=78$ sites (and $\delta^{\text{eff}}=22$ sites). Because this value is larger than the size of our simulated array, we further include the results of simulations with smaller values for the penetration depth. In part due to the ratio $\delta(\omega_{\text{pump}})/\delta^{\text{eff}} \gg 1$, the effects of the penetration depth on the fluence dependence of τ , I_∞ , and α are small.

XIII. SIMULATED CLUSTER PROPERTIES

Better understanding of the PIPT in CRO and related compounds may come from future experimental investigations of the photoinduced clusters. In Fig. S13 we present the number of clusters and the average cluster size of the L_c and S_c states found in our simulations once site-switching has stopped (using the same simulation settings as used in the main text, i.e. a $40 \times 40 \times 40$ array with $\sigma_{th} = 3$ and $\beta = 0$). A cluster here is defined as a collection of sites possessing the same state (i.e. L_c or S_c) connected by an unbroken chain of nearest neighbor links.

Figures S14 and S15 show the time-dependence of the cluster sizes and the number of clusters, respectively, of both the L_c and S_c phases in the simulation presented in the main text (i.e. a $40 \times 40 \times 40$ array with $\sigma_{th}=3$ and $\beta=0$).

The sigmoid-like dependence of the cluster size on the fluence, and the time dependence of the cluster sizes could be observed in future experiments using time-resolved diffuse x-ray or electron diffraction to verify our model of the photo-induced insulator-metal transition as a percolation phenomenon.

XIV. TEMPERATURE EFFECTS

To ensure that the sample fully recovered between pulses, we varied the repetition rate of the laser (both pump and probe pulses) and fixed the probe pulse to arrive shortly before the pump pulse, while keeping the pump and probe fluences fixed. If the sample fully recovers between pulses, $I^{2\omega}$ will exhibit a linear trend with the repetition rate (because the intensity is proportional to the number of probe pulses), while a sublinear trend indicates an incomplete recovery of the sample between pump pulses. Figure S16 shows $I^{2\omega}$ vs. the repetition rate for the largest pump fluence used in this experiment, 1.3 mJ/cm^2 . We see that at repetition rates above the 5 kHz used in the experiment, the sample no longer recovers between pulses of this fluence. This is verified by performing a linear fit (with zero offset) to the data points ≤ 5 kHz.

A. Transient pump-induced heating

From the heat capacity, we can determine an upper bound on the transient increase in the lattice temperature following the pump pulse. To do this, we use the following expression:

$$q = \int_{T_i}^{T_f} dT c(T), \quad (\text{S18})$$

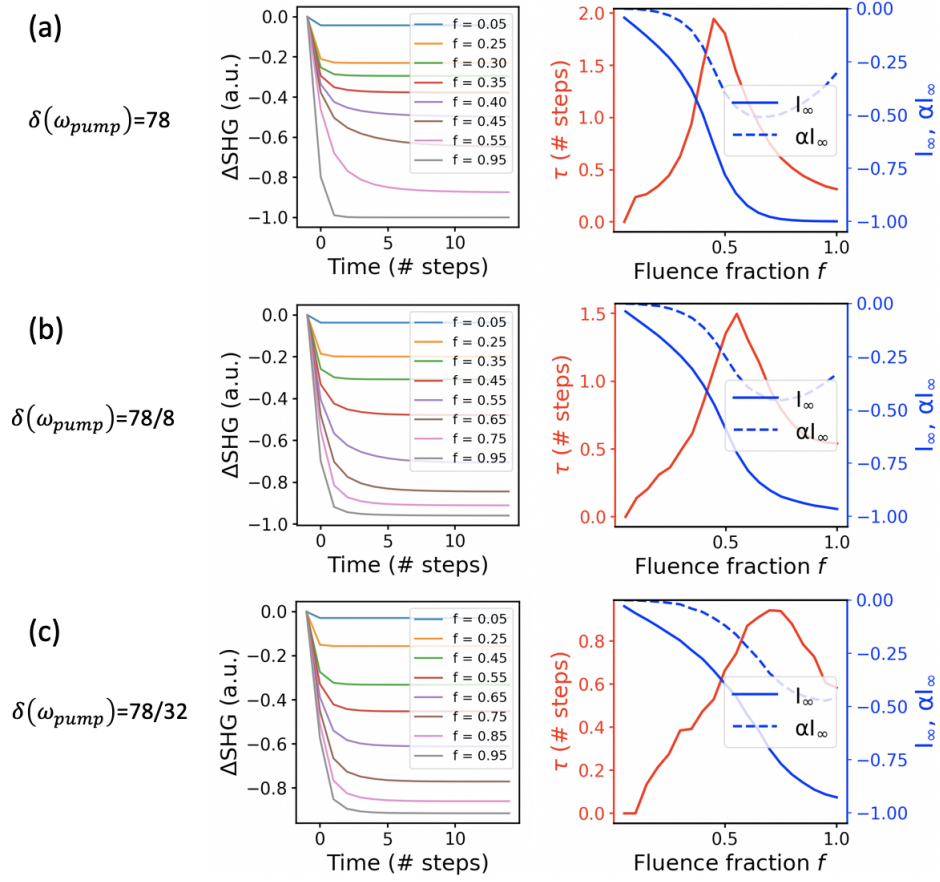


FIG. S12. Simulation output accounting for the penetration depth of the pump $\delta(\omega_{pump})$ and of the probe δ^{eff} . The ratio $\delta(\omega_{pump})/\delta^{eff}=3.5$ is fixed in all cases. **(a-c)** show the results for $\delta(\omega_{pump})$ set to 78, 9.8, and 2.4 sites, respectively.

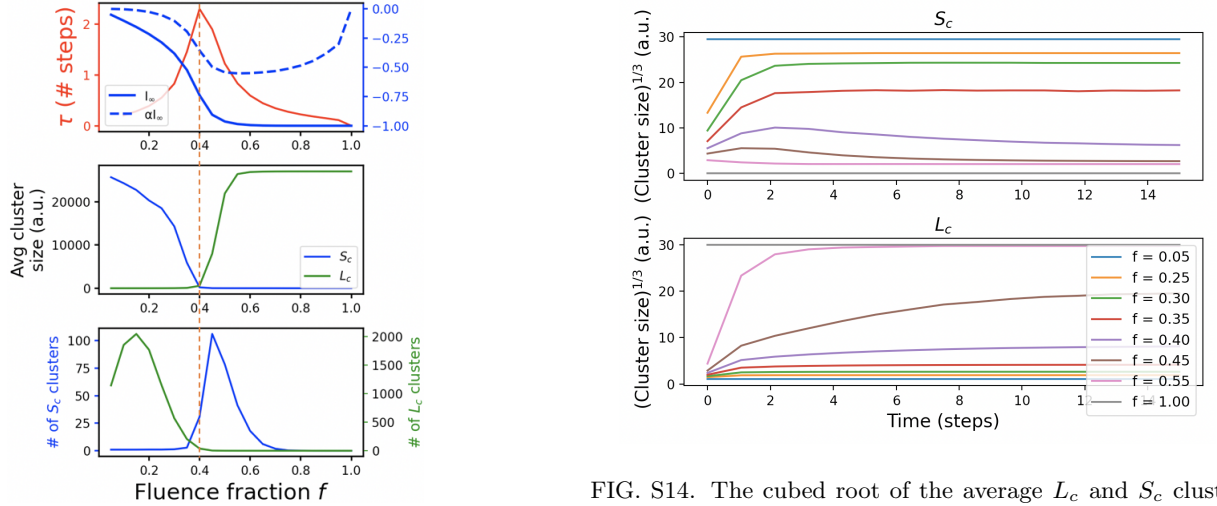


FIG. S13. Cluster behavior in the 40x40x40 simulation with $\sigma_{th}=3$ and $\beta=0$. **(top)** Reproduction of Fig. 3(b) for comparison: τ , I_∞ , and αI_∞ vs. fluence fraction f **(middle)** Average area of the simulated S_c and L_c clusters at $t \rightarrow \infty$ vs. fluence fraction **(bottom)** number of S_c and L_c clusters at $t \rightarrow \infty$ in the simulations

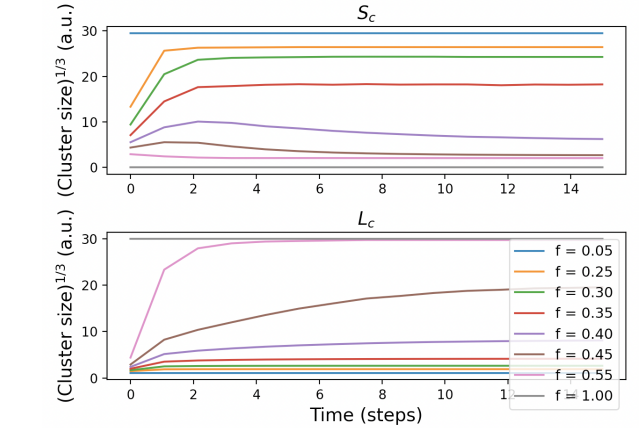


FIG. S14. The cubed root of the average L_c and S_c cluster sizes vs. time steps in the 3d simulations with $\sigma_{th}=3$ and $\beta=0$.

where q is the average heat absorbed per unit cell from a single pulse, $T_{i(f)}$ is the initial(final) lattice temperature, and $c(T)$ is the heat capacity per unit cell. The heat capacity as a function of temperature is extracted from

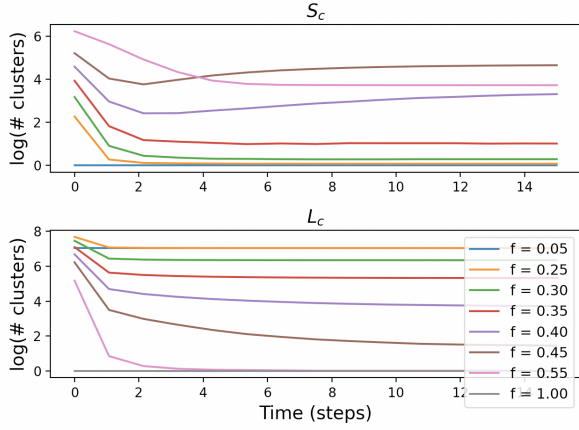


FIG. S15. The logarithm of the average number of L_c and S_c clusters vs. time steps in the 3d simulations with $\sigma_{th}=3$ and $\beta=0$.

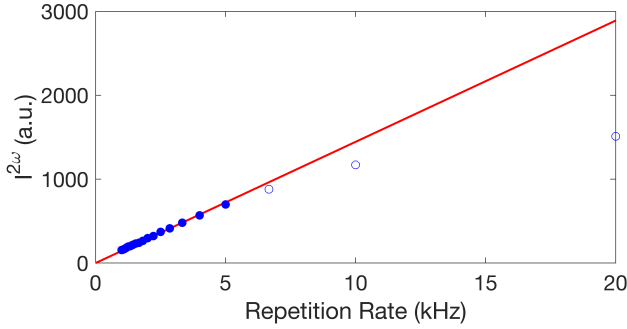


FIG. S16. $I^{2\omega}$ shortly before the arrival of a 1.2 mJ/cm² pump pulse vs. repetition rate of the pump and probe pulses. The red line is a linear fit (with zero offset) to the filled data points. The data included in the text was taken at 5 kHz.

Ref. [11], which used a flux-grown sample (as was used in our measurements). Specifically, this allows us to extract coefficients for the T and T^3 terms in $c(T)$.

The following equation gives the absorbed energy per unit cell q , calculated with a weighted average in which the weight is proportional to the probe sensitivity:

$$\begin{aligned}
 q &= (1 - R)F \frac{V_{uc}}{\delta(\omega_{pump})} \frac{\int_0^\infty dz e^{-z/\delta(\omega_{pump})} e^{-z/\delta^{eff}}}{\int_0^\infty dz e^{-z/\delta(\omega_{pump})}} \\
 &= (1 - R)F \frac{V_{uc}}{\delta(\omega_{pump})} \frac{1}{1 + \frac{\delta^{eff}}{\delta(\omega_{pump})}},
 \end{aligned}
 \tag{S19}$$

where $\delta(\omega) = 78$ nm is the penetration depth of the pump beam, $\delta^{eff} = 22$ nm is the effective penetration depth of

the SHG probe (c.f. Eq. S17), F is the fluence of the pump pulse, and $R = .18$ is the reflectivity at the pump wavelength.

The upper bound on the transient temperature T_f following the pump pulse is determined by equating these two expressions for the absorbed energy per unit cell q .

The only remaining parameter in this calculation is the crystal temperature before the arrival of the pump pulse T_i . Without laser heating, the crystal is at a nominal temperature of ≈ 4 K. From Fig. 1(a), we see that the steady-state temperature increase due to the probe laser is ≈ 2 K near the transition temperature T_{MI} . However, at lower temperatures the heat capacity is smaller and the steady-state temperature increase due to the probe beam will be larger. But, because we are interested in obtaining an upper bound for the transient temperature increase, it suffices to assume a large initial temperature due to the heating from the probe laser. Table II presents the obtained upper bound on the transient lattice temperature T_f immediately following the pump pulse for various initial temperatures and for fluences $F_{sat} = 0.4$ mJ/cm² and $F_{max} = 1.2$ mJ/cm².

T_i (K)	T_f @ $F = F_{sat}$ (K)	T_f @ $F = F_{max}$ (K)
10	31	41
20	32	42
25	34	43

TABLE II. Upper bounds on the lattice temperature T_f immediately following the arrival of the pump laser pulse for pump fluences $F_{sat} = 0.4$ mJ/cm² and $F_{max} = 1.2$ mJ/cm² and several initial steady-state temperatures T_i .

B. Temperature-dependent time traces

The complete data set corresponding to Fig. 2(b) with pump fluence 0.28 mJ/cm² is shown in Figure S17(b). Comparison with the data shown in S17(a) serves to highlight the variation in these measurements. Fig. S17(a) shows a very long relaxation timescale at temperatures just below the transition. However, no similar trend appears in Fig. S17(b), where time traces at temperatures near the transition are flat after several ps and have values between those at temperatures far above and below the transition. As mentioned previously, the domain structure along the c axis has an effect on the measured SHG [2], and this may be related to the differences between the datasets presented here.

XV. LANDAU THEORY FOR SHG NEAR THE METAL-INSULATOR TRANSITION

We develop a Landau theory for the metal-insulator transition at $T_{MI}=48$ K. (Laser heating is ignored in this discussion.) Our main purpose is to calculate the in-plane components of the SHG susceptibility tensor, $\chi_{ijk}^{ED} \equiv \chi_{ijk}$ (where i, j, k take values in $\{a, b\}$), for T near T_{MI} .

To describe the transition itself, independent of its relation to SHG, we postulate that a symmetry-preserving order parameter η undergoes a first-order phase transition at $T = T_{MI}$. In this part of the calculation, we follow Ref. [12], in which a Landau theory is developed for a symmetry-preserving order parameter (see also Ref. [13]).

The symmetry-preserving order parameter in our calculation is intended to describe the change in crystal structure at the transition and could be, for instance, the volume change of the unit cell. The microscopic nature of this order parameter does not affect the calculations below. Indeed, the calculation below seems to be equally applicable if the order parameter is instead taken to describe the change in electronic structure, since this is also symmetry-preserving. However, as discussed in the main text, experimental evidence from the Fe-doped compound disfavors either the electronic or magnetic structural change as explanations for the jump in SHG.

To describe SHG, we provide two phenomenological approaches, neither of which we attempt to justify microscopically, but both of which yield the same phenomenological parameterization of the measured quantity $I^{2\omega}$. In the first approach, we expand the SHG susceptibility in the order parameter η . Here we have taken inspiration from the Landau calculation of elastoresistivity in Ref. [14]. In the second approach, we use a phenomenological time-averaged Landau free energy that includes frequency dependence, following and extending the approach of Refs. [15, 16]. Ref. [16] has developed this approach for the case of a symmetry-breaking order parameter; in this case, certain SHG tensor components must vanish above the transition temperature by symmetry, but can be non-vanishing below the transition temperature because the order parameter reduces the symmetry. In the case we consider, the same SHG tensor components are allowed both above and below T_{MI} (since the transition does not break any symmetries), and we describe this in an approach that goes beyond that of Ref. [16] in that we explicitly minimize over frequency-dependent internal degrees of freedom in the time-averaged Landau free energy.

We organize the calculation as follows. First, we review the symmetry-preserving transition as developed by Ref. [12]. Second, we discuss how symmetries constrain the tensor elements of the SHG susceptibility. Then we present two phenomenological approaches to obtaining the jump in $I^{2\omega}$.

A. Symmetry-preserving transition

We recall here the Landau theory provided by Kuznetsov et al. [12] for a generic symmetry-preserving phase transition. Taking η to be a symmetry-preserving order parameter, one writes

$$\mathcal{F}_0 = a_1\eta + a_2\eta^2 + a_3\eta^3 + \eta^4. \quad (\text{S20})$$

The cubic term is eliminated by the change of variables $\Delta = \eta + a_3/4$, $\tilde{a}_1 = a_1 + a_3^3/8 - a_2a_3/2$, $\tilde{a}_2 = a_2 - \frac{3}{8}a_3^2$, yielding $\mathcal{F}_0 = \tilde{a}_1\Delta + \tilde{a}_2\Delta^2 + \Delta^4$, where a Δ -independent constant has been dropped. The solutions to $\partial\mathcal{F}_0/\partial\Delta = 0$ are presented in Ref. [12]. The final result that we need for the present calculation is that if $D \equiv 8\tilde{a}_2^3 + 27\tilde{a}_1^2 < 0$ (note that this requires $\tilde{a}_2 < 0$), then \mathcal{F}_0 is an asymmetric double well, with the global minimum being on the left if $\tilde{a}_1 > 0$ and on the right if $\tilde{a}_1 < 0$. Ref. [12] presents three solutions (in the case $D < 0$) called Δ_1 , Δ_2 , and Δ_3 . We find (contrary to Ref. [12]) that the global minimum is Δ_1 , i.e., the solution defined by

$$\Delta_1 \equiv -2\rho \cos \frac{\varphi}{3}, \quad (\text{S21})$$

where $\rho = \text{sgn} \tilde{a}_1 \sqrt{|\tilde{a}_2|/6}$ and $\varphi = \arccos\left(\frac{\tilde{a}_1}{8\rho^3}\right)$ (note that φ is real because of $D < 0$). To get a first order phase transition for our problem, we fix $\tilde{a}_2 < 0$ and assume a linear dependence on temperature near T_{MI} :

$$\tilde{a}_1 = \tilde{a}_{1,0}(T - T_{MI}), \quad (\text{S22})$$

where $\tilde{a}_{1,0}$ is a temperature-independent constant. Then Δ_1 (and thus also the equilibrium value of the original order parameter η) jumps discontinuously at $T = T_{MI}$.

For later convenience, we write the global minimum in an alternate form with the temperature dependence explicitly included:

$$\Delta_1(T) = -\sqrt{\frac{|\tilde{a}_2|}{2}} \left[\text{sgn}(\tilde{a}_{1,0}(T - T_{MI})) + f(\tilde{a}_{1,0}(T - T_{MI})) \right], \quad (\text{S23})$$

where $f(x)$ is a smooth function defined by

$$f(x) = \begin{cases} \frac{2}{\sqrt{3}} \cos \left(\frac{1}{3} \arccos \left[\frac{1}{8} \left(\frac{|\tilde{a}_2|}{6} \right)^{-3/2} x \right] \right) - 1 & 0 < x < \left(\frac{2}{3} |\tilde{a}_2| \right)^{3/2}, \\ -f(-x) & -\left(\frac{2}{3} |\tilde{a}_2| \right)^{3/2} < x < 0. \end{cases} \quad (\text{S24})$$

We note in particular the expansion of $\Delta_1(T)$ near $T = T_{MI}$:

$$\Delta_1(T) = -\sqrt{\frac{|\tilde{a}_2|}{2}} \left[\text{sgn}(\tilde{a}_{1,0}(T - T_{MI})) + \frac{\tilde{a}_{1,0}(T - T_{MI})}{2\sqrt{2}|\tilde{a}_2|^{3/2}} \right] + O((T - T_{MI})^2). \quad (\text{S25})$$

Thus, at the transition temperature, $\Delta_1(T)$ jumps discontinuously with a continuous slope whose sign at $T = T_{MI}$ is the same as the sign of the discontinuity [i.e., $\Delta_1(T)$ resembles either Fig. S18 or the same figure flipped vertically]. The global minimum $\eta_0(T)$ of the original order parameter is then obtained by the additive shift $\eta_0(T) = \Delta_1(T) - a_3/4$.

From Eq. (S25), we see that, in order to obtain a consistent expansion to linear order in $T - T_{MI}$, it may be necessary to include temperature dependence in some of the coefficients (a_2 and a_3) that we took as constant in Eq. (S20), i.e., set $\tilde{a}_2 = \tilde{a}_{2,0} + \tilde{a}_{2,1}(T - T_{MI}) + O((T - T_{MI})^2)$ (with $\tilde{a}_2 < 0$ always) and $a_3 = a_{3,0} + a_{3,1}(T - T_{MI}) + O((T - T_{MI})^2)$. Eq. (S25) then would yield

$$\eta_0(T) = A + B \text{sgn}(T - T_{MI}) + C(T - T_{MI}) + D|T - T_{MI}| + O((T - T_{MI})^2), \quad (\text{S26})$$

where A, B, C, D are temperature-independent constants [e.g., $A = -\sqrt{|\tilde{a}_{2,0}|/2} \text{sgn} \tilde{a}_{1,0}$]. In other words, $\eta_0(T)$ jumps discontinuously and its slope can be different on either side of the jump.

For the expansion (S20) to make sense, the order parameter must be small [e.g., we should have $|B| \ll |A|$ in (S26)]. A strongly first order transition would not necessarily fit into this framework.

B. Symmetry-allowed components of the SHG susceptibility tensor

Next, we recall how inversion symmetry along a particular axis is broken in CRO through the scenario of hybrid improper ferroelectricity [17–20]. It is convenient to consider the components of the polar moment along the crystallographic axes $\hat{\mathbf{a}} \equiv [110]$ and $\hat{\mathbf{b}} \equiv [\bar{1}10]$:

$$P_a \equiv \mathbf{P} \cdot \hat{\mathbf{a}}, \quad P_b \equiv \mathbf{P} \cdot \hat{\mathbf{b}}. \quad (\text{S27})$$

In the following discussion, we use the notation and results of Harris (Ref. [18]). While Ref. [18] focuses on $\text{Ca}_3\text{Mn}_2\text{O}_7$ and $\text{Ca}_3\text{Ti}_2\text{O}_7$, we can expect CRO to fit into the same framework.

The key point is that the full symmetry of the reference tetragonal structure $I4/mmm$ is broken down to $Cmc2_1$ (#36) by the condensation of an octahedral tilt mode and an octahedral rotation mode. [We note here that $Cmc2_1$ is an alternative expression for the space group $Bb2_1m$ mentioned in the main text; see footnote 13 in Ref. [21].] Furthermore, there is a symmetry-allowed trilinear coupling between the tilt mode, rotation mode, and polar moment. There are 8 possible domains: first there are two choices for the wavevector \mathbf{q} associated with both the tilt and rotation mode, and then there four choices corresponding to the tilt mode and rotation mode each have an independently chosen sign. The spontaneous polar moment lies either along the a axis or b axis with either sign, so the 8 domains correspond to four possible directions for the spontaneous polar moment, i.e., 90 degree domains. (Recall that we focused in the experiment on a region of the sample in which any domains present, whether one or more than one, were aligned along a single axis. However, 90 degree domains were observed in other samples.) We note that, up to an overall constant (which is of no concern since we only wish to establish the axis along which inversion is broken), we may identify the x and y components of \mathbf{P} with $Q_{5,1}$ and $Q_{5,2}$ from Ref. [18]. Thus, again up to an overall constant, our P_a and P_b are Z_5 and $-Y_5$ from Ref. [18]. See Eq. (7) of Ref. [18] for the trilinear coupling.

The condensation of these order parameters described above occurs at some temperature much higher than the transition T_{MI} that is our focus. For our purpose of studying T near T_{MI} , we only need to note that inversion is broken along the axis of the spontaneous polar moment (either a or b , depending on the domain). The symmetries that mix a and b components together (see Table II and Eq. (2) of Ref. [18]) are also broken. We thus see that the symmetry-allowed tensor elements of the SHG susceptibility are as in (S2).

From here on, we focus on the three tensor elements relevant to the experimental geometry, namely, χ_{aba}, χ_{baa} , and χ_{bbb} (note that $\chi_{aab} = \chi_{aba}$). Also, we consider only the case of a uniform sample (no domains).

C. First approach: direct expansion

For the regime of T near T_{MI} that is our focus, we can obtain a phenomenological expression for the SHG susceptibility by supposing that it is analytic in the symmetry-preserving order parameter η . In particular, we write

$$\chi_{ijk} = A_{ijk}^{(\omega)} + B_{ijk}^{(\omega)}\eta + O(\eta^2), \quad (\text{S28})$$

where $(ijk) = (aba), (baa)$, or (bbb) and where $A_{ijk}^{(\omega)}, B_{ijk}^{(\omega)}$ are constants (possibly complex) that could depend on temperature as well as frequency. This approach has some similarity to the Landau theory calculation of elastoelasticity in Ref. [14], though the symmetry considerations here are different.

It is simplest to assume that $A_{ijk}^{(\omega)}, B_{ijk}^{(\omega)}$ are smooth functions of temperature (at least for T near T_{MI}). Then, the discontinuous jump in the equilibrium value $\eta_0(T)$ as T crosses T_{MI} (see Sec. XV A) yields a corresponding jump in each χ_{ijk} (weighted by the appropriate coefficient $B_{ijk}^{(\omega)}$ evaluated at $T = T_{MI}$). In this way, we have related a first-order, symmetry-preserving phase transition with a jump in SHG susceptibility.

D. Second approach: Time-averaged Landau free energy

We now present another phenomenological calculation of the SHG susceptibility for T near T_{MI} . Here, the assumption (S28) is replaced by two other assumptions: (a) neglect of dissipation and (b) the existence of a time-averaged Landau free energy (see below). This approach yields the same phenomenological parameterization (of χ_{ijl}) as the approach of Sec. XV C except with real coefficients instead of complex, due to the assumption (a).

In Ref. [15], Pershan proposed a phenomenological ‘‘time-averaged free energy’’ function that includes frequency dependence and can be used to calculate nonlinear optical effects. In Ref. [16], Sa et al. extended this approach further by including coupling to an order parameter in the time-averaged free energy. The time-averaged free energy as considered by Ref. [16] is a frequency-dependent analogue to the usual (frequency-independent) equilibrium free energy; it is sufficient for determining whether or not a particular tensor component of the SHG susceptibility is or is not constrained to be zero above a symmetry-breaking transition temperature. Since in our present problem we are considering a transition that does not break any symmetries, we must develop the approach of Ref. [16] further in order to calculate the change in tensor components that are symmetry-allowed both above and below the transition. To do this, we use a frequency-dependent analogue to the usual (frequency-independent) Landau free energy. The essential difference with [16], then, is that we explicitly minimize over frequency-dependent degrees of freedom of the system.

1. SHG in a toy model

As a warm-up, we consider a toy model of SHG (with no temperature dependence or phase transition): a one-dimensional model without inversion symmetry. The sample is subject to external electric fields at frequencies ω and 2ω . We write the amplitudes of the AC electric field and polar moment at frequency ω' ($\omega' = \omega$ or 2ω) as $E^{(\omega')}$ and $P^{(\omega')}$. For a more careful discussion of the order of limits used in defining these Fourier amplitudes, see Eq. (2.8) and below in Ref. [15].

The AC polar moments, which are the internal variables of the system, appear in all terms allowed by symmetry. We have already accounted for translation symmetry by writing the electric fields and polar moments as position-independent quantities. The only remaining symmetry of this toy model is time translation. Under time translation by t' , $P^{(\omega')} \rightarrow e^{it'\omega'} P^{(\omega')}$ and $P^{(\omega')*} \rightarrow e^{-it'\omega'} P^{(\omega')*}$, which implies that in any given term, the sum of frequencies in unconjugated polar moments must equal the sum of frequencies in conjugated polar moments. For the time-averaged Landau free energy, we thus write the most general polynomial (up to fourth order) that satisfies time translation invariance:

$$\mathcal{F}_{AC}^{(\text{toy})} = \sum_{\omega'=\omega,2\omega} (a^{(\omega')} |P^{(\omega')}|^2 + \frac{1}{2} b^{(\omega')} |P^{(\omega')}|^4) + c^{(\omega)} |P^{(\omega)}|^2 |P^{(2\omega)}|^2 + 2\text{Re}[d^{(\omega)} P^{(2\omega)*} (P^{(\omega)})^2], \quad (\text{S29})$$

in which $a^{(\omega')}$, $b^{(\omega')}$, $c^{(\omega)}$, and $d^{(\omega)}$ are constants. Although a complex $d^{(\omega)}$ is consistent with symmetry and with $\mathcal{F}_{AC}^{(\text{toy})}$ being real, an imaginary part seems to result either in dissipation (contrary to the basic assumption of the approach [15]) or in unphysical effects, so hereafter we assume that $d^{(\omega)}$ is real. On physical grounds, we also assume

that the parameters in $\mathcal{F}^{(\text{toy})}$ are such that the AC polar moment vanishes in the absence of an external electric field; for instance, $a^{(\omega')}$, $b^{(\omega')}$, and $c^{(\omega')}$ should all be positive.

Including the coupling between the polar moment and the external electric field, we obtain:

$$\mathcal{F}^{(\text{toy})} = \mathcal{F}_{\text{AC}}^{(\text{toy})} + \mathcal{F}_{\text{ext}}, \quad (\text{S30})$$

where

$$\mathcal{F}_{\text{ext}} = \sum_{\omega'=\omega, 2\omega} \left(-E^{(\omega')} P^{(\omega)'} - E^{(\omega')*} P^{(\omega)'} \right). \quad (\text{S31})$$

The minimum of $\mathcal{F}^{(\text{toy})}$ (varying the real and complex parts of $P^{(\omega)}$ and $P^{(2\omega)}$) is then a function of $(E^{(\omega)}, E^{(2\omega)})$ only and coincides with the time-averaged free energy considered by Ref. [16].

We proceed to calculate the linear susceptibility and SHG susceptibility in this toy model. It is convenient to minimize in $P^{(\omega)}$ and $P^{(2\omega)}$ with $P^{(\omega)*}$ and $P^{(2\omega)*}$ treated as independent variables. (This is equivalent to minimizing in the real and complex parts of $P^{(\omega)}$ and $P^{(2\omega)}$.) To present the calculation more compactly, we define 4-component arrays:

$$\underline{P} = (P^{(\omega)}, P^{(\omega)*}, P^{(2\omega)}, P^{(2\omega)*}), \quad (\text{S32a})$$

$$\underline{E} = (E^{(\omega)}, E^{(\omega)*}, E^{(2\omega)}, E^{(2\omega)*}). \quad (\text{S32b})$$

The minimization condition may be written as $\partial\mathcal{F}^{(\text{toy})}/\partial\underline{P}^* = 0$, i.e.,

$$\underline{E} = \frac{\partial\mathcal{F}_{\text{AC}}^{(\text{toy})}}{\partial\underline{P}^*}. \quad (\text{S33})$$

The polar moment that minimizes $\mathcal{F}^{(\text{toy})}$ may generally be expanded

$$\underline{P}_\alpha = (\chi_1)_{\alpha\beta} \underline{E}_\beta + (\chi_2)_{\alpha\beta\gamma} \underline{E}_\beta \underline{E}_\gamma + \dots, \quad (\text{S34})$$

where repeated indices are summed (from 1 to 4) and where \underline{P}^s is the spontaneous polar moment and χ_1, χ_2 are the first- and second-order susceptibility tensors. The SHG susceptibility is a particular component of χ_2 :

$$\chi_{\text{SHG}} = \frac{1}{2} \frac{\partial^2 P^{(2\omega)}}{\partial(E^{(\omega)})^2} \Big|_{\underline{E}=0} = (\chi_2)_{311}. \quad (\text{S35})$$

To calculate the susceptibilities, we write the 4-by-4 matrix $\partial\underline{P}_\alpha/\partial\underline{E}_\beta$ as $\partial\underline{P}/\partial\underline{E}$ and use a simple matrix identity:

$$\frac{\partial\underline{P}}{\partial\underline{E}} = \left(\frac{\partial\underline{E}}{\partial\underline{P}} \right)^{-1}. \quad (\text{S36})$$

Then we get $\chi_1 = (\partial\underline{E}/\partial\underline{P})^{-1}|_{\underline{P}=0} = \text{diag}(\chi_1^{(\omega)}, \chi_1^{(\omega)}, \chi_1^{(2\omega)}, \chi_1^{(2\omega)})$, where $\chi_1^{(\omega')} = 1/a^{(\omega')}$ [c.f. Eqs. (S29) and (S33)].

To get the second-order susceptibility, we expand $\partial\underline{E}/\partial\underline{P}$ to another order:

$$\frac{\partial\underline{E}}{\partial\underline{P}} = \chi_1^{-1} + \frac{\partial^2 \underline{E}}{\partial\underline{P}_\alpha \partial\underline{P}} \underline{P}_\alpha + \dots, \quad (\text{S37})$$

where the omitted terms are quadratic or higher in \underline{P} . Then

$$\left(\frac{\partial\underline{E}}{\partial\underline{P}} \right)^{-1} = \chi_1 - \chi_1 \frac{\partial^2 \underline{E}}{\partial\underline{P}_\alpha \partial\underline{P}} \chi_1 \underline{P}_\alpha + \dots, \quad (\text{S38})$$

which yields the SHG susceptibility:

$$\chi_{\text{SHG}} = \frac{1}{2} \left\{ \frac{\partial\underline{P}_\alpha}{\partial E^{(\omega)}} \frac{\partial}{\partial\underline{P}_\alpha} \left[\left(\frac{\partial\underline{E}}{\partial\underline{P}} \right)^{-1} \right]_{31} \right\} \Big|_{\underline{P}=0} \quad (\text{S39a})$$

$$= \frac{1}{2} \left\{ \chi_1^{(\omega)} \frac{\partial}{\partial P^{(\omega)}} \left[-\chi_1^{(2\omega)} \frac{\partial^2 E^{(2\omega)}}{\partial\underline{P}_\alpha \partial P^{(\omega)}} \chi_1^{(\omega)} \underline{P}_\alpha \right] \right\} \Big|_{\underline{P}=0} \quad (\text{S39b})$$

$$= -\frac{1}{2} \chi_1^{(2\omega)} (\chi_1^{(\omega)})^2 \frac{\partial^2 E^{(2\omega)}}{\partial^2 P^{(\omega)}} \Big|_{\underline{P}=0} \quad (\text{S39c})$$

$$= -d^{(\omega)} \chi_1^{(2\omega)} (\chi_1^{(\omega)})^2. \quad (\text{S39d})$$

2. SHG near the metal-insulator transition in CRO

Next, we combine the above ingredients into a time-averaged Landau free energy that describes the SHG susceptibility tensor in CRO near the transition at T_{MI} .

As our focus is on the in-plane (i.e., the a - b plane) susceptibility, we ignore the c axis. We write the most general time-averaged Landau free energy consistent with inversion symmetry along a (but broken inversion along b) and time translation invariance, keeping only up to quartic terms:

$$\mathcal{F} = \mathcal{F}_0 + \mathcal{F}_{AC} + \mathcal{F}_{\text{coupling}} + \mathcal{F}_{\text{ext}}, \quad (\text{S40})$$

where \mathcal{F}_0 is the Landau free energy for the symmetry-preserving order parameter η [Eq. (S20)], and where

$$\begin{aligned} \mathcal{F}_{AC} = \sum_{i=a,b} \left[\sum_{\omega'=\omega,2\omega} \left(a_i^{(\omega')} |P_i^{(\omega')}|^2 + \frac{1}{2} b_i^{(\omega')} |P_i^{(\omega')}|^4 \right) + c_{ij}^{(\omega)} |P_i^{(\omega)}|^2 |P_j^{(2\omega)}|^2 \right] \\ + 2\text{Re}[2d_{aba}^{(\omega)} P_a^{(2\omega)*} P_a^{(\omega)} P_b^{(\omega)} + d_{baa}^{(\omega)} P_b^{(2\omega)*} (P_a^{(\omega)})^2 + d_{bbb}^{(\omega)} P_b^{(2\omega)*} (P_b^{(\omega)})^2], \end{aligned} \quad (\text{S41a})$$

$$\begin{aligned} \mathcal{F}_{\text{coupling}} = \sum_{i=a,b} \sum_{\omega'=\omega,2\omega} \left(\beta_i^{(\omega')} \eta |P_i^{(\omega')}|^2 + \lambda_i^{(\omega')} \eta^2 |P_i^{(\omega')}|^2 \right) \\ + 2\text{Re}[2\delta_{aba}^{(\omega)} \eta P_a^{(2\omega)*} P_a^{(\omega)} P_b^{(\omega)} + \delta_{baa}^{(\omega)} \eta P_b^{(2\omega)*} (P_a^{(\omega)})^2 + \delta_{bbb}^{(\omega)} \eta P_b^{(2\omega)*} (P_b^{(\omega)})^2], \end{aligned} \quad (\text{S41b})$$

$$\mathcal{F}_{\text{ext}} = \sum_{i=a,b} \sum_{\omega'=\omega,2\omega} 2\text{Re}[-P_i^{(\omega')*} E_i^{(\omega')}]. \quad (\text{S41c})$$

The a and b components of the polar moment and electric field are defined as in Eq. (S27), now with frequency dependence. The quantities $a_i^{(\omega')}$, $b_i^{(\omega')}$, $c_{ij}^{(\omega)}$, $d_{ijk}^{(\omega)}$ are all temperature-independent constants (as are a_2 and a_3 in \mathcal{F}_0). The only temperature dependence in \mathcal{F} is in the term \tilde{a}_1 that drives the first-order phase transition in η . As in the toy model of the previous section, we assume that the constants are such that the spontaneous AC polar moment is zero.

The linear susceptibility and SHG susceptibilities are found similarly as in the toy model. The arrays of polar moments and electric fields acquire an additional index specifying the component in the a - b plane:

$$\underline{P} = (P_a^{(\omega)}, P_b^{(\omega)}, P_a^{(\omega)*}, P_b^{(\omega)*}, P_a^{(2\omega)}, P_b^{(2\omega)}, P_a^{(2\omega)*}, P_b^{(2\omega)*}), \quad (\text{S42a})$$

$$\underline{E} = (E_a^{(\omega)}, E_b^{(\omega)}, E_a^{(\omega)*}, E_b^{(\omega)*}, E_a^{(2\omega)}, E_b^{(2\omega)}, E_a^{(2\omega)*}, E_b^{(2\omega)*}). \quad (\text{S42b})$$

The minimization conditions are $\partial\mathcal{F}/\partial\eta = 0$ and $\partial\mathcal{F}/\partial P_\alpha = 0$, the second of which yields the electric field as a function of polar moment:

$$\underline{E}_\alpha = \frac{\partial(\mathcal{F}_{AC} + \mathcal{F}_{\text{coupling}})}{\partial P_\alpha^*}. \quad (\text{S43})$$

We note that the η -dependent terms in \mathcal{F} may be brought to the form

$$\mathcal{F}_0 + \mathcal{F}_{\text{coupling}} = a_1(\underline{P})\eta + a_2(\underline{P})\eta^2 + a_3\eta^3 + \eta^4, \quad (\text{S44})$$

where

$$\begin{aligned} a_1(\underline{P}) = a_1 + \sum_{i=a,b} \sum_{\omega'=\omega,2\omega} \beta_i^{(\omega')} |P_i^{(\omega')}|^2 \\ + 2\text{Re}[\delta_{aba}^{(\omega)} P_a^{(2\omega)*} P_a^{(\omega)} P_b^{(\omega)} + \delta_{baa}^{(\omega)} P_b^{(2\omega)*} (P_a^{(\omega)})^2 + \delta_{bbb}^{(\omega)} P_b^{(2\omega)*} (P_b^{(\omega)})^2], \end{aligned} \quad (\text{S45a})$$

$$a_2(\underline{P}) = a_2 + \sum_{i=a,b} \sum_{\omega'=\omega,2\omega} \lambda_i^{(\omega')} |P_i^{(\omega')}|^2 \quad (\text{S45b})$$

The minimization in η thus yields a value $\eta_0(T, \underline{P})$ that can be obtained by replacing $a_1 \rightarrow a_1(\underline{P})$ and $a_2 \rightarrow a_2(\underline{P})$ in the solution found in Sec. XV A. Note that $\eta_0(T, \underline{0}) = \eta_0(T)$ [where $\eta_0(T) = \Delta_1(T)$ with $\Delta_1(T)$ given by Eqs. (S23)-(S25)]. Also note that since \underline{P} appears at least quadratically in $a_1(\underline{P})$ and $a_2(\underline{P})$, we have

$$\left. \frac{\partial\eta(\underline{P})}{\partial P_\alpha} \right|_{\underline{P}=\underline{0}} = 0. \quad (\text{S46})$$

As in the toy model case, we calculate the first-order and SHG susceptibilities using Eq. (S36) (which is now an 8-by-8 matrix equation). From $\chi_1 = (\partial P / \partial E)|_{P=0}$, Eqs. (S41a)-(S41b) and (S43) yield

$$\chi_1 \leftrightarrow \text{diag}(\chi_1^{(\omega)}, \chi_1^{(\omega)}, \chi_1^{(\omega)}, \chi_1^{(\omega)}, \chi_1^{(2\omega)}, \chi_1^{(2\omega)}, \chi_1^{(2\omega)}, \chi_1^{(2\omega)}), \quad (\text{S47})$$

where

$$\chi_1^{(\omega')} = \frac{1}{a^{(\omega')} + \beta^{(\omega')} \eta_0(T) + \lambda^{(\omega')} \eta_0(T)^2}. \quad (\text{S48})$$

By the same manipulations as in the toy model case, we obtain the in-plane components of the SHG susceptibility tensor:

$$\chi_{ijk} = - \left[d_{ijk}^{(\omega)} + \delta_{ijk}^{(\omega)} \eta_0(T) \right] \chi_1^{(2\omega)} (\chi_1^{(\omega)})^2, \quad (\text{S49})$$

where $(ijk) = (aba), (baa),$ or (bbb) .

Dividing out the first-order susceptibilities yields:

$$\frac{\chi_{ijk}}{\chi_1^{(2\omega)} (\chi_1^{(\omega)})^2} = A_{ijk}^{(\omega)} + B_{ijk}^{(\omega)} \Delta_1(T), \quad (\text{S50})$$

where $A_{ijk}^{(\omega)}$ and $B_{ijk}^{(\omega)}$ are temperature-independent constants determined by the various constants appearing in \mathcal{F} . The temperature dependence of $\Delta_1(T)$ is discussed in Sec. XVA.

Furthermore, since in truncating \mathcal{F} to quartic order we have already assumed η to be a small parameter (note that this means \tilde{a}_2 must be small), we may expand Eq. (S48) in $\eta_0(T)$. Collecting the various constants, we find that χ_{ijk} itself (even without dividing the first-order susceptibilities) also takes the form of the right-hand side of Eq. (S50) (with different constants $A_{ijk}^{(\omega)}, B_{ijk}^{(\omega)}$).

* tcabin@g.ucla.edu

- [1] M. Fiebig, V. V. Pavlov, and R. V. Pisarev, *J. Opt. Soc. Am. B* **1**, 96 (2005).
- [2] S. Lei, M. Gu, D. Puggioni, G. Stone, J. Peng, J. Ge, Y. Wang, B. Wang, Y. Yuan, K. Wang, Z. Mao, J. M. Rondinelli, and V. Gopalan, *Nano Lett.* **18**, 3088–3095 (2018).
- [3] J. S. Lee, S. J. Moon, B. J. Yang, J. Yu, U. Schade, Y. Yoshida, S.-I. Ikeda, and T. W. Noh, *Phys. Rev. Lett.* **98**, 097403 (2007).
- [4] A. Zong, P. E. Dolgirev, A. Kogar, E. Ergeçen, M. B. Yilmaz, Y.-Q. Bie, T. Rohwer, I.-C. Tung, J. Straquadine, X. Wang, Y. Yang, X. Shen, R. Li, J. Yang, S. Park, M. C. Hoffmann, B. K. Ofori-Okai, M. E. Kozina, H. Wen, X. Wang, I. R. Fisher, P. Jarillo-Herrero, and N. Gedik, *Phys. Rev. Lett.* **123**, 097601 (2019).
- [5] A. S. McLeod, A. Wieteska, G. Chiriaco, B. Foutty, Y. Wang, Y. Yuan, F. Xue, V. Gopalan, L. Q. Chen, Z. Q. Mao, A. J. Millis, A. N. Pasupathy, and D. N. Basov, *npj Quantum Materials* **6** (2021).
- [6] D. Perez-Salinas, A. S. Johnson, D. Prabhakaran, and S. Wall, *Nature Communications* **13** (2022).
- [7] R. H. Schonmann, *The Annals of Probability* **20**, 174 (1992).
- [8] J. Balogh, B. Bollobás, H. Duminil-Copin, and R. Morris, *Trans Am Math Soc* **364**, 2667 (2012).
- [9] J. Balogh, B. Bollobás, and R. Morris, *Ann. Probab.* **37**, 1329 (2009).
- [10] A. E. Holroyd, *Probability Theory and Related Fields* **125**, 195 (2003).
- [11] V. Varadarajan, S. Chikara, V. Durairaj, X. Lin, G. Cao, and J. Brill, *Solid State Communications* **141**, 402 (2007).
- [12] A. Y. Kuznetsov, V. P. Dmitriev, O. I. Bandilet, and H.-P. Weber, *Physical Review B* **68**, 064109 (2003).
- [13] G. Azzolina, R. Bertoni, C. Ecolivet, H. Tokoro, S.-i. Ohkoshi, and E. Collet, *Physical Review B* **102**, 134104 (2020).
- [14] M. C. Shapiro, P. Hlobil, A. T. Hristov, A. V. Maharaj, and I. R. Fisher, *Physical Review B* **92**, 235147 (2015).
- [15] P. S. Pershan, *Physical Review* **130**, 919 (1963).
- [16] D. Sa, R. Valentí, and C. Gros, *The European Physical Journal B - Condensed Matter and Complex Systems* **14**, 301 (2000).
- [17] N. A. Benedek and C. J. Fennie, *Physical Review Letters* **106**, 107204 (2011).
- [18] A. B. Harris, *Physical Review B* **84**, 064116 (2011).
- [19] N. A. Benedek, A. T. Mulder, and C. J. Fennie, *Journal of Solid State Chemistry* **195**, 11 (2012).
- [20] E. A. Nowadnick and C. J. Fennie, *Physical Review B* **94**, 104105 (2016).
- [21] Y. Yoshida, S.-I. Ikeda, H. Matsuhata, N. Shirakawa, C. H. Lee, and S. Katano, *Phys. Rev. B* **72**, 054412 (2005).

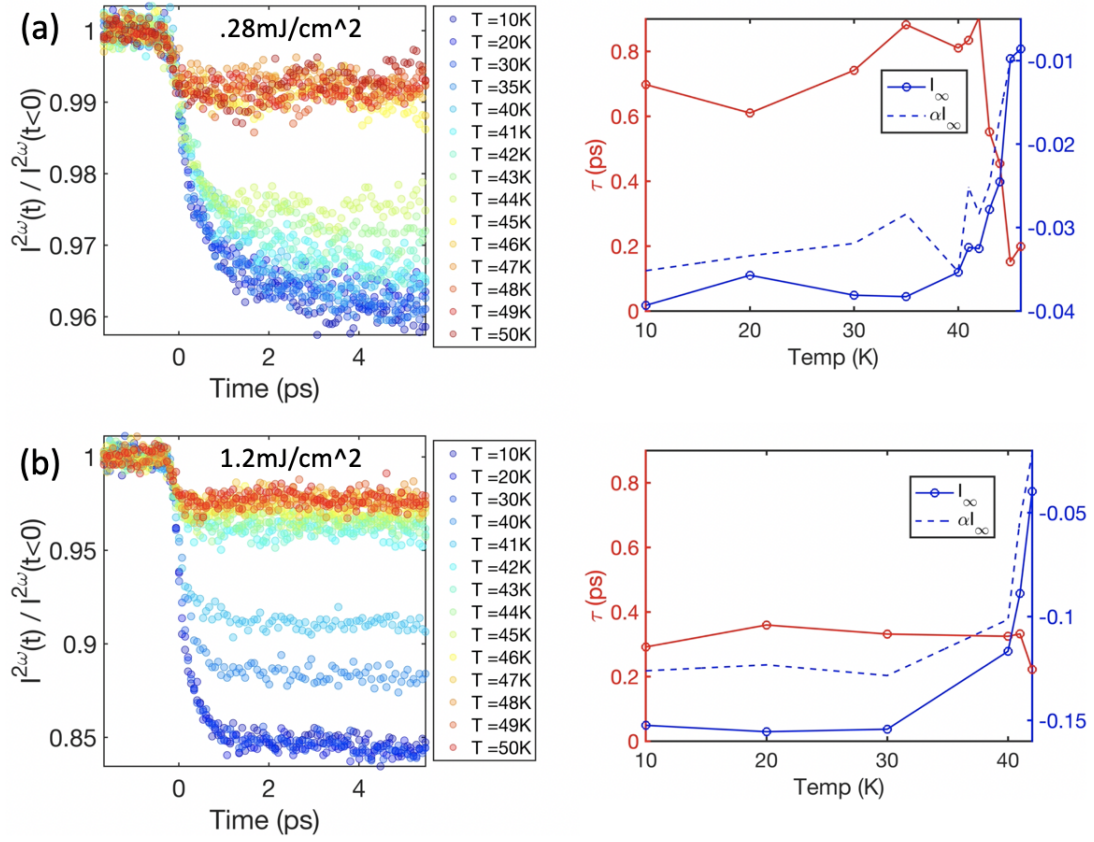


FIG. S17. SHG time traces at varying temperature and the corresponding fit parameters extracted from fitting to Eq. 1. **(a)** The pump fluence is fixed at 0.28 mJ/cm² and the polarization is such that $I^{2\omega} \propto |\chi_{baa}^{ED}|^2$. **(b)** The pump fluence is 1.2 mJ/cm² and the polarization is such that $I^{2\omega} \propto |\chi_{bbb}^{ED}|^2$. The two datasets were taken at different locations on the sample.

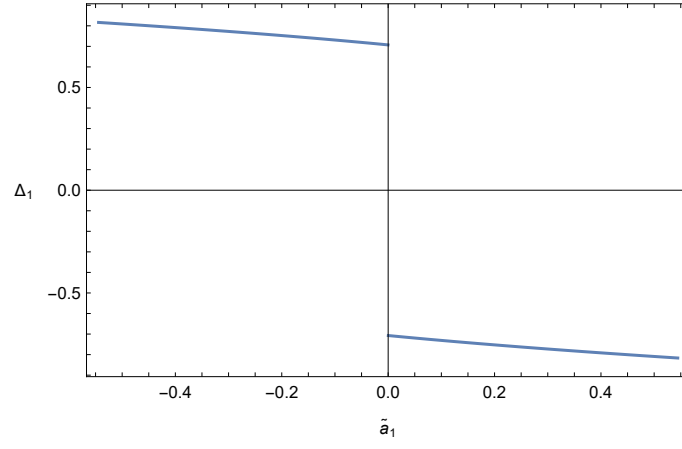


FIG. S18. The global minimum Δ_1 for $\tilde{a}_2 = -1$ (all units are arbitrary).